

THE H I KINEMATICS AND DISTRIBUTION OF FOUR BLUE COMPACT DWARF GALAXIES¹

TRINH X. THUAN

Astronomy Department, University of Virginia, P.O. Box 3818, University Station, Charlottesville, VA 22903; txt@virginia.edu

J. E. HIBBARD

National Radio Astronomy Observatory, 520 Edgemont Road, Charlottesville, VA 22903; jhibbard@nrao.edu

AND

FRANÇOIS LÉVRIER

Astronomy Department, University of Virginia, P.O. Box 3818, University Station, Charlottesville, VA 22903; francois.levrier@obspm.fr

Received 2003 November 3; accepted 2004 May 6

ABSTRACT

We present VLA H I observations of the blue compact dwarf (BCD) galaxies NGC 2366, NGC 4861, VII Zw 403, and Haro 2. These galaxies span a range of BCD morphological types. The cometary-like BCDs NGC 2366 and NGC 4861 have regular rotational kinematics with a V/σ of 8.7 and 6.4, respectively. On the other hand, the velocity fields of the iE BCD VII Zw 403 and of the nE BCD Haro 2 lack regularity, and their rotational motion is around the major, not the minor, axis. The H I distribution is centrally peaked in VII Zw 403 and Haro 2, a general feature of all iE and nE-type BCDs, the most common ones. In contrast, cometary-type BCDs have multiple H I peaks that are scattered over the disk. The active regions of star formation are associated with regions of high H I column densities, with slight displacements between the H I and stellar peaks. NGC 2366 shows many H I minima, resulting from the disruptive influence of massive star formation and supernovae on the interstellar medium (ISM). In NGC 2366 and NGC 4861, there is a tendency for H I gas with a higher velocity dispersion to be associated with regions of lower H I column density. This anticorrelation can be understood in the context of a two-phase model of the ISM. In all BCDs, the radio continuum emission is associated with the star-forming regions and is predominantly thermal in nature. H I clouds with no optical counterparts have been found in the vicinity of NGC 4861 and Haro 2.

Key words: galaxies: individual (NGC 2366, NGC 4861, VII Zw 403, Haro 2) — galaxies: kinematics and dynamics — galaxies: starburst

1. INTRODUCTION

Blue compact dwarf (BCD) galaxies are low-luminosity galaxies ($M_B \geq -18$) that are currently undergoing an intense burst of star formation. Their metallicities range between $\frac{1}{50}$ and $\frac{1}{3}$ of that of the Sun, implying that they are chemically relatively young. Izotov & Thuan (1999) have argued that the most metal-deficient BCDs with abundance $12 + \log(\text{O}/\text{H}) \leq 7.6$ (or $Z \leq Z_\odot/20$) may be genuine young galaxies, with stars not older than several hundred megayears. This makes BCDs unique laboratories for studying the burst mode of star formation and nucleosynthesis processes by massive stars in very metal-deficient environments, not unlike those prevailing at the time of galaxy formation.

Despite much observational and theoretical work (see, e.g., Thuan et al. 1998), there are still many unanswered questions concerning BCDs. In particular, the triggering mechanism of the starbursts in BCDs is still not known. Single-dish H I surveys of BCDs (e.g., Thuan & Martin 1981, hereafter TM81; Thuan et al. 1999; Salzer et al. 2002; Lee et al. 2002) have shown BCDs to contain substantial amounts (10^8 – $10^9 M_\odot$) of neutral gas. H I interferometric studies of the kinematics of the neutral gas can shed light not only on how starbursts get triggered but also on such questions as: Are the motions of the neutral gas dominated by rotation or turbu-

lence? What is the amount of dark matter in BCDs? What is the relationship between the H I and optical components? Does star formation always occur at locations where the Toomre (1964) criterion for gravitational instability is satisfied? What type of constraints can the kinematics of the H I gas put on scenarios of BCDs evolving to other types of dwarf galaxies such as dwarf irregulars (dIs) or dwarf ellipticals (dEs)?

Previous H I interferometric work on BCDs (Lequeux & Viallefond 1980; Viallefond & Thuan 1983; Viallefond et al. 1987; Lo et al. 1993; Taylor et al. 1994; van Zee et al. 1998a, 1998b; Simpson & Gottesman 2000; Pustilnik et al. 2001; Young et al. 2003) has brought partial answers to some of these questions. Here we examine some of these issues anew by studying the H I distribution and kinematics in four BCDs selected from the BCD catalog of TM81. To examine how these properties depend on the optical morphological structure, the BCDs were chosen to span a range of BCD morphological types as defined by Loose & Thuan (1985) on the basis of optical images. Two of the BCDs, NGC 2366 and NGC 4861, belong to the rare class of “cometary” (C) galaxies (the iI,C type, where i denotes the irregular shape of the star-forming region and I the irregular shape of the extended underlying stellar component) characterized by a high surface brightness starburst (the comet’s “head”) at one end of their elongated low surface brightness (LSB) stellar bodies (the comet’s “tail”). The third BCD, VII Zw 403, of type iE, has a irregular (i) star-forming region near the center of the galaxy embedded within an elliptical (E) halo, while the fourth, Haro 2 \equiv Mrk 33 \equiv UGC 5720, with the classification nE, possesses a nuclear (n) star-forming region at

¹ Based on observations obtained at the National Radio Astronomy Observatory, a facility of the National Science Foundation, operated under cooperative agreement by Associated Universities, Inc.

TABLE 1
GLOBAL PROPERTIES

Parameters	NGC 2366	NGC 4861	VII Zw 403	Haro 2	Reference
BCD Type.....	iI,C	iI,C	iE	nE	1
α (J2000).....	07 28 54.96	12 59 01.78	11 28 00.40	10 32 31.93	2
δ (J2000).....	69 12 56.6	34 51 39.7	78 59 35.9	54 24 03.5	2
l (deg).....	146.42	11.52	127.84	156.20	2
b (deg).....	28.54	82.10	37.33	52.80	2
V_{HI} (km s ⁻¹).....	96	833	-92	1454	3
D (Mpc).....	3.44	10.7	4.5	24.5	4
i (deg) ^a	59	82	5
D_{25} (arcsec) ^b	487.7	238.9	86.7	60	6
r_{25} ^b	0.41	0.37	0.57	0.93	6
B_T^{oc}	11.03	12.60	14.10	13.39	6
$M_{B_T}^{\text{oc}}$	-16.65	-17.54	-14.17	-18.56	6
$(S_{\text{HI}}^e dv)_{\text{SD}}$ (Jy km s ⁻¹) ^d	205.7	42.4	14.4	4.4	5
ΔV_{50} (km s ⁻¹).....	99	92	43	113	3
ΔV_{20} (km s ⁻¹).....	126	125	54	153	3
M_{HI} (10 ⁹ M _⊙).....	0.57	1.14	0.069	0.62	5
M_T (10 ⁹ M _⊙).....	1.86	1.84	0.088	1.56	5
L_B (10 ⁹ L _⊙) ^e	0.71	1.61	0.072	4.13	6
M_T/L_B	2.62	1.14	1.22	0.38	5
M_{HI}/L_B	0.80	0.71	0.96	0.15	5
M_{HI}/M_T	0.31	0.62	0.78	0.40	5

NOTE.—Units of right ascension are hours, minutes, and seconds, and units of declination are degrees, arcminutes, and arcseconds.

^a Inclinations derived in this paper for NGC 2366 and NGC 4861.

^b Angular diameter and axial ratio measured to the B surface brightness level of 25 mag arcsec⁻².

^c Total face-on RC3 magnitudes corrected for Galactic and internal extinction. For NGC 4861, we adopt a Galactic extinction of 0.05 mag (Schlegel et al. 1998) and an internal extinction of 0.25 mag (Izotov et al. 1997).

^d Flux from Thuan & Martin (1981) corrected for beam size using their equation (12) and the H I sizes measured in this work. The flux for NGC 4861 is derived from a new 140 foot (43 m) single-dish spectrum.

^e Adopting $M_{B_T, \odot}^0 = 5.48$.

REFERENCES.—(1) Loose & Thuan 1985; (2) NED; (3) TM81; (4) Tolstoy et al. 1995 (NGC 2366), Heckman et al. 1998 (NGC 4861 and Haro 2), Lynds et al. 1998 (VII Zw 403); (5) this paper; (6) RC3 (de Vaucouleurs et al. 1991).

the center of an extended underlying stellar component with elliptical (E) isophotes.

The global optical and H I properties of the four BCDs taken from TM81 and the RC3 (de Vaucouleurs et al. 1991) are listed in Table 1. To derive accurate absolute quantities, care was exercised in choosing the best possible distance determinations for each BCD. NGC 2366 has a Cepheid-determined distance of 3.44 Mpc (Tolstoy et al. 1995), while Tikhonov et al. (1991) derive a distance of 3.4 Mpc from photometry of its brightest stars, and Thuan & Izotov (2004) obtained a distance of 3.3 ± 0.3 Mpc from the tip of the red giant branch. We adopt the Cepheid-derived distance of 3.44 Mpc, which places NGC 2366 in the M81 group. Using the Virgocentric infall model of Schechter (1980) with parameters $\gamma = 2$, $v_{\text{Virgo}} = 976$ km s⁻¹, $w_{\odot} = 220$ km s⁻¹, and $D(\text{Virgo}) = 15.9$ Mpc, then the distance of Mrk 59 is 10.7 Mpc (Heckman et al. 1998). As for VII Zw 403, its distance is 4.5 Mpc as determined from the tip of the red giant branch (Schulte-Ladbeck et al. 1998; Lynds et al. 1998). For Haro 2, we adopt the distance of 24.5 Mpc derived by Heckman et al. (1998) using the same Virgocentric infall model as for Mrk 59. We describe the observations in § 2, present our results in § 3, and list our conclusions in § 4.

2. OBSERVATIONS AND DATA REDUCTION

The H I observations were conducted between 1984 and 1992 with the VLA in its spectral-line mode. Each galaxy was observed in the 3 km C configuration, resulting in a resolution of $\sim 15''$. Because of the lack of short baselines, this configuration is insensitive to emission distributed smoothly on scales

greater than $4'$ per channel. The field-of-view is set by the 25 m diameter of the individual array elements and amounts to $30'$ full width at half-maximum (FWHM). A description of the VLA is given by Napier et al. (1983).

Because of limitations of the correlator at the time, the data obtained in 1984 and 1986 (concerning NGC 2366 and Haro 2, respectively) consist of 12 hr tracks taken in the single intermediate frequency (IF) (2A) mode. Data taken in 1992 (NGC 4861 and VII Zw 403) consist of 9 hr tracks taken in the dual IF (2AC) mode. A total bandwidth of 1.56 MHz was used in each case, and online Hanning smoothing was applied to the data after which every other channel was discarded, leaving a set of independent channels, or a velocity “data cube.” The resulting velocity cubes consist of 31 channels each of width 10.4 km s⁻¹ for the older data, and 127 channels each of width 2.6 km s⁻¹ for the 1992 data. The observational parameters are summarized in Table 2.

Standard VLA editing and calibration procedures via observations of the standard VLA calibrator 3C 286 were followed (e.g., Fomalont & Perley 1999; Rupen 1999). The resulting images are nearly thermal noise limited, except for NGC 2366, as is discussed later (§ 3.1). The data were mapped using the robust weighting technique of Briggs (1995). The data cube with a robust parameter $R = -1$ allows for finer resolution at the expense of fainter extended structures. These “high-resolution” cubes are used to characterize the kinematics of each system. The $R = 1$ “low-resolution” data cube trades resolution for better surface brightness sensitivity and is used to characterize the general H I morphology. The parameters for

TABLE 2
VLA OBSERVING AND MAP DETAILS

Parameter	NGC 2366	NGC 4861	VII Zw 403	Haro 2
Date	1984 Apr 23	1992 Apr 11	1992 Apr 11	1986 Oct 27
Configuration	C	C	C	C
Correlator mode	2A	2AC	2AC	2A
Number of antennae	25	27	27	27
Time on source (min)	538	266	226	456
Flux calibrator	3C 286	3C 286	3C 286	3C 286
Phase calibrator	071+439	3C 286	1039+811	1031+567
Central velocity (km s ⁻¹)	+96	+835	-60	+1450
Bandwidth (MHz)	1.56	1.56	1.56	1.56
Number of channels	31	127	127	31
Channel spacing (km s ⁻¹)	10.3	2.6	2.6	10.4
Map Parameters				
Continuum:				
Robust factor	-1	-1	-1	-1
Resolution (arcsec, FWHM)	12.5 × 11.5	15.2 × 11.6	17.2 × 11.0	14.1 × 12.9
Noise (mJy beam ⁻¹)	0.37	0.25	0.22	0.33
High resolution:				
Robust factor	-1	-1	-1	-1
Resolution (arcsec, FWHM)	12.5 × 11.5	15.2 × 11.6	17.2 × 11.0	14.1 × 12.9
Noise (mJy beam ⁻¹)	1.1	1.2	1.8	1.2
Noise (10 ¹⁹ cm ⁻²)	8.7	1.9	2.7	7.6
Low resolution:				
Robust factor	+1	+1	+1	+1
Resolution (arcsec, FWHM)	16.6 × 14.6	18.6 × 14.5	21.2 × 14.5	19.2 × 17.1
Noise (mJy beam ⁻¹)	0.78	1.1	1.3	0.84
Noise (10 ¹⁹ cm ⁻²)	3.7	1.1	1.2	2.9

the high- and low-resolution maps are listed in Table 2. Finally, to increase our sensitivity to even fainter extended structures, the $R = 1$ cubes were smoothed to resolution of $35'' \times 35''$ and by a factor of 2–4 in velocity. These maps are used to measure the total H I flux recovered by the interferometer. The three maps are referred to as the high-resolution, low-resolution, and smoothed maps.

The mapped data cubes were examined to determine the channels containing spectral line emission (ignoring the few channels on either end of the cube where the spectral response of the receiver is less than 90% of the peak response). The continuum was then subtracted from the entire u - v data cube by making a linear fit to the visibility data over the line-free channels on either side of the bandpass (Cornwell et al. 1992). A spectra-line data cube was made by mapping the continuum-subtracted data cube, and a line-free continuum image was made by averaging together the line-free channels and mapping with a robust parameter $R = -1$. Finally, these maps were CLEANed to remove the antenna sampling pattern (Clark 1980).

The data cubes were integrated over the velocity axis to produce the moment maps (Rupen 1999). It should be noted that the moment 1 and 2 maps give an accurate representation of the mean H I velocity and line-of-sight velocity dispersion at a location (α, δ) only if the line profiles are single peaked at that location.

3. RESULTS

3.1. General Presentation

For each system, we illustrate the global H I morphology and kinematics and the relationship to the underlying starlight.

Two sources of optical images were used: either the Digitized Sky Survey² (DSS) or CCD images in the B band. DSS images were used for the mosaics of NGC 2366 (Fig. 1) and NGC 4861 (Fig. 7) and their channel maps (Figs. 3 and 10), and for the channel maps of VII Zw 403 (Fig. 19). The CCD images were used in all other cases. The CCD data are described in Noeske et al. (2000) for NGC 2366 and NGC 4861, in Papaderos et al. (1994) for VII Zw 403, and in Loose & Thuan (1986) for Haro 2.

For each galaxy we present a six panel mosaic (Fig. 1 for NGC 2366, Fig. 7 for NGC 4861, Fig. 17 for VII Zw 403, and Fig. 21 for Haro 2). In each mosaic, the upper panels show the optical image with both a deep (*left*) and shallow (*right*) stretch of the transfer function. The former gives a better idea of the total optical extent of the system, while the latter shows the location of the brighter star-forming regions within the galaxy. The middle panels of the mosaic present the H I intensity map (moment 0) made from the low-resolution data cubes, superposed on the optical image (*left*) and as gray scales (*right*). Finally, the lower panels show the isovelocity contour (moment 1, *left*) and velocity dispersion (moment 2, *right*) maps made from the high-resolution data cubes, with dark and light gray scales indicating higher and lower velocities, respectively. The contours on the moment 1 map are

² The Second Palomar Observatory Sky Survey was made by the California Institute of Technology with funds from the National Science Foundation, the National Geographic Society, the Sloan Foundation, the Samuel Oschin Foundation, and the Eastman Kodak Corporation. The Oschin Schmidt Telescope is operated by the California Institute of Technology and Palomar Observatory.

TABLE 3
H I MEASURED PROPERTIES FROM THE VLA MAPS

Parameter	NGC 2366	NGC 4861	VII Zw 403	Haro 2
$S_{1.4 \text{ GHz}}$ (mJy) ^a	11.7	10.0	2.5	19.0
$a_G \times b_G$ (arcsec) ^b	92.8×65.5	224×61	77.2×51.6	73.6×29.3
$(a \times b)_{\text{low}}$ (arcsec) ^c	705×255	345×125	175×115	86×37
$(a \times b)_{\text{smoothed}}$ (arcsec) ^d	815×265	405×275	215×175	110×55
$(S_{\text{HI}} dv)_{\text{VLA}}$ (Jy km s ⁻¹) ^e	138.4	38.4	11.0	3.4
$(S_{\text{HI}} dv)_{\text{VLA}} / (S_{\text{HI}}^c dv)_{\text{SD}}$	0.67	0.91	0.76	0.77
$M_{\text{HI}}^{\text{VLA}}$ ($10^8 M_{\odot}$).....	3.9	10.4	0.52	4.8
$\Delta V_{50}^{\text{VLA}}$ (km s ⁻¹).....	109.6	80.0	34.1	90.4
$\Delta V_{20}^{\text{VLA}}$ (km s ⁻¹).....	126.9	113.1	50.4	150.0
$V_{\text{rot}} \sin i$ (km s ⁻¹) ^e	61.1	51.1	20:	65:
V_{rot} (km s ⁻¹) ^e	67	54	<20	<65
$\langle \sigma \rangle$ (km s ⁻¹) ^f	7.7	8.4	7.8	16.1
$V_{\text{rot}} / \langle \sigma \rangle$	8.7	6.4	<2.5	<4.0
σ_{peak} (km s ⁻¹).....	14.3	19	12.7	31.9

^a The flux listed for NGC 2366 is the sum of the fluxes of Mrk 71 and of the H II region to the east of it.

^b Deconvolved H I sizes used in equation (12) of TM81 and derived by fitting an elliptical Gaussian to the smoothed intensity H I map.

^c Deconvolved H I sizes measured from the low-resolution maps at a H I column density of 10^{20} cm^{-2}

^d Deconvolved H I sizes measured from the higher sensitivity maps smoothed to a resolution of $35''$ at a H I column density of $5 \times 10^{19} \text{ cm}^{-2}$. Note that the smoothed size of NGC 2366 is a lower limit as our H I map does not fully sample the H I emission. Hunter et al. 2001 measured a total H I extent about twice as large.

^e For NGC 2366 and NGC 4861, the maximum rotational velocity around the minor axis was derived from fitting a tilted-ring model to the intensity map. For VII Zw 403 and Haro 2, the rotation appears to be around the major axis, and the more uncertain maximum rotational velocity is derived from position-velocity cuts along the minor axis.

^f Derived as the mean velocity dispersion of the second-moment map.

isovelocity contours, while those in the moment 2 map represent H I column densities from the high-resolution data.

Following the mosaics, we present a more detailed view of specific regions in each system, showing the relationship between radio and optical features, using the higher resolution H I data (Fig. 2 for NGC 2366, Fig. 8 for NGC 4861, Fig. 18 for VII Zw 403, and Fig. 22 for Haro 2). The leftmost panels plot the 1.4 GHz radio continuum on a gray-scale rendering of the optical image. The middle panels show the high-resolution H I column density on the optical image, and the rightmost panels show the H I column density on a gray-scale representation of the high-resolution velocity dispersion map, with light shades corresponding to small H I line widths and dark shades to large line widths.

Next we present channel maps of each system (Fig. 3 for NGC 2366, Fig. 10 for NGC 4861, Fig. 19 for VII Zw 403, and Fig. 23 for Haro 2). In these, the H I emission is contoured on a gray-scale representation of the optical image, and only channels showing H I emission are plotted.

The integrated H I spectrum for each source is given in Figure 6. In this figure, the emission measured from the low-resolution data cube is plotted with a short dashed line, the emission measured from the smoothed data cube is plotted with a long dashed line, and the raw emission measured by a single-dish telescope (TM81) is plotted with a solid line.

In order to compare the integrated fluxes measured with the interferometer to those measured with the single-dish telescope, the single-dish fluxes need to be corrected for the coupling between the extended H I distribution and the single-dish beam. The corrected single-dish (SD) flux S_c is calculated from the observed flux S assuming that the H I has a Gaussian spatial distribution with major and minor axes (FWHM) a_G and b_G , via equation (12) of TM81. To estimate a_G and b_G , we

fit an elliptical Gaussian to the smoothed intensity maps. The corrected single-dish flux³ $(S_{\text{HI}}^c dv)_{\text{SD}}$ is tabulated in Table 1, while a_G and b_G , the integrated VLA flux, $(S_{\text{HI}} dv)_{\text{VLA}}$, and the ratios of the VLA to single-dish flux are tabulated in Table 3. For each galaxy, we also give in Table 3 two measures of the H I extent: $(a \times b)_{\text{low}}$ measured from the low-resolution H I maps (Fig. 1c, Fig. 7c, Fig. 17c, and Fig. 21c) at a H I column density of $1 \times 10^{20} \text{ cm}^{-2}$, and $(a \times b)_{\text{smoothed}}$ measured from the more sensitive smoothed H I maps (resolution of $35''$) at a column density of $5 \times 10^{19} \text{ cm}^{-2}$. Both sets of sizes have been beam deconvolved.

For NGC 4861, the VLA and single-dish fluxes are equal within the errors. For the other galaxies, the interferometer does not recover as much flux as the single-dish telescope. This could partly be due to uncertainties in the absolute calibration of the single-dish measurements, which are thought to be accurate to only $\sim 15\%$ (cf. van Zee et al. 1997). It may also be due in part to the lack of short baselines in the VLA C configuration, which makes the interferometer insensitive to emission that is smooth on scales greater than $\sim 4'$ in a single velocity channel (see especially discussion of NGC 2366 [§ 3.2]). This corresponds to physical scales of 4.0, 12.5, 5.2, and 28.6 kpc for NGC 2366, NGC 4861, VII Zw 403, and Haro 2, respectively. This means that we are unable to detect any extended envelopes, like those discovered around the BCD I Zw 18 (van Zee et al. 1998b) or the dlrr galaxy NGC 4449 (Hunter et al. 1998).

³ These values differ from previously reported single-dish fluxes, since prior to these mapping observations the true H I distribution was unknown. Instead, a_G and b_G were estimated using a statistical relationship between the H I and optical diameters of mapped systems.

For each system, we model the velocity field by fitting tilted rings and a Brandt rotation curve (Dickel & Rood 1978) to the moment 1 map. The kinematic center and systemic velocity were held fixed at values determined from position-velocity profiles taken along the major axis of the high-resolution H I data. Using the AIPS program *GAL*, we then used the low-resolution H I data to fit for the position angle of the receding edge (PA), the inclination of the galaxy's plane on the line of sight (i), and the rotation curve as characterized by the maximum velocity V_m , the radius where maximum velocity is reached, R_m , and the index n , which describes the shape of the rotation curve in a Brandt (1960) model. Deprojected rotation curves are given for NGC 2366 (Fig. 4) and NGC 4861 (Fig. 12). We could find no acceptable solutions for VII Zw 403 or Haro 2.

We now discuss each system individually.

3.2. NGC 2366 and Mrk 71

NGC 2366 is a dwarf irregular galaxy, which can also be classified as a cometary galaxy in the classification scheme of Loose & Thuan (1985). The high surface brightness supergiant H II region Mrk 71 \equiv NGC 2363 at the southwestern end of the galaxy is the head of the comet, while its low surface brightness body is its tail. At the distance of 3.44 Mpc, 1'' in NGC 2366 corresponds to 17 pc.

Abundance determinations (e.g., Izotov et al. 1997; Noeske et al. 2000) of Mrk 71 give an oxygen abundance $12 + \log(\text{O}/\text{H}) \sim 7.9$, or $\frac{1}{10}$ solar. Roy et al. (1996) have measured the oxygen abundance $12 + \log(\text{O}/\text{H})$ in several other H II regions in the main body of NGC 2366 to be between 8.1 and 8.3, slightly higher than in Mrk 71. Using photometric and spectroscopic observations, Noeske et al. have concluded that the age of the oldest stars in NGC 2366 does not exceed ~ 3 Gyr, making it a relatively young galaxy. Thuan & Izotov (2004) have used *Hubble Space Telescope* (*HST*) V and I images to perform a color-magnitude diagram (CMD) analysis of the stellar populations in NGC 2366. The CMD reveals not only young stellar populations such as blue main-sequence stars and blue and red supergiants, but also an older evolved stellar population of red giant and relatively bright asymptotic giant branch stars, indicating star formation has occurred from about 2 Gyr ago, consistent with the age estimate of Noeske et al. (2000).

Hunter et al. (2001) have reported VLA H I C and D configuration observations of NGC 2366. Because of the much better sampling of short baselines in the D configuration data, their observations do not suffer from the negative "bowl" of missing flux that our observations are subject to (as described below), and their observations more accurately reproduce the smooth extended emission in NGC 2366. However, our high-resolution maps have a finer resolution than theirs by a factor of 2.5, and in that sense are complementary to the Hunter et al. maps. Braun (1995) presented VLA B+C+D configuration maps of NGC 2366 at 6'', 9'', and 65'' resolutions but gave no detailed description of those data.

3.2.1. H I Morphology

The results for NGC 2366 are shown in Figures 1–5. The most prominent feature of the H I distribution is its clumpiness (see in particular Fig. 1d). There are several H I peaks, with densities as high as $3 \times 10^{21} \text{ cm}^{-2}$, as well as some very distinct density minima. Overall, there is a large variation in the H I column density on scales of a few hundred parsecs (see also Fig. 2), indicative of a disturbed medium.

In a global sense, there is a correlation between the H I column density peaks and regions of active star formation. Comparison of Figures 1c and 1d shows that the southernmost H I peak corresponds closely to Mrk 71. There are other H I clumps that are also associated with young star clusters: the two northeast of Mrk 71 and the one west of the supergiant H II region. However, while their H I column densities are comparable to that of Mrk 71, the star formation in these regions are not as intense. In fact, $\sim 70\%$ of the total H α emission of NGC 2366 comes from Mrk 71 alone (Hunter et al. 2001).

However, association does not mean a perfect correspondence between the H I and optical peaks. A closer look at the region around Mrk 71 shows that they are actually somewhat displaced (Fig. 2b), with the maximum H I column density displaced to the east of Mrk 71 by ~ 1 beamwidth (~ 250 pc). The change in column density is $4 \times 10^{21} \text{ cm}^{-2}$ between Mrk 71 and the gas peak ($6 \times 10^{21} \text{ cm}^{-2}$) to the east. Hunter et al. (2001) reported a similar shift between the H I and H α peaks. This might arise from a bulk displacement of the H I as a result of sweeping of the neutral medium by supernovae and stellar winds, in addition to an increase in the gas ionization fraction at the location of Mrk 71. We can check whether such a bulk displacement can be explained by the mechanical energy deposited in the ISM of the galaxy by the energy release from massive stars via stellar winds and supernova explosions. Roy et al. (1991) have observed a superbubble blowout in Mrk 71 and have estimated the mechanical energy deposited in the ISM by stellar winds of massive stars to drive the expansion of the superbubble to be $3.1 \times 10^{39} \text{ ergs s}^{-1}$. Because its kinematic age is only 2×10^6 yr, the mechanical energy provided by supernovae (SNe) to drive this particular superbubble is negligible.

We can estimate the mechanical energy deposited by SNe in Mrk 71 by using the star formation rate (SFR) derived for high-mass stars ($M \geq 10 M_\odot$) by Drissen et al. (2000) to be equal to $0.02 M_\odot \text{ yr}^{-1}$. Adopting a Salpeter initial mass function $dN/dM \propto M^{-\alpha}$ ($M_l = 10 M_\odot$, $M_u = 120 M_\odot$, and $\alpha = 2.35$), this SFR implies an upper limit for the SN rate of $8.6 \times 10^{-4} \text{ yr}^{-1}$. Taking the kinetic energy input of each SN to be 10^{51} ergs , then an upper bound to the SN mechanical energy input is $2.7 \times 10^{40} \text{ ergs s}^{-1}$. Evidently, the contribution of SNe to the mechanical energy released in the ISM is much more important than that of stellar winds. According to Weaver et al. (1977), in the standard superbubble model, the time evolution of the radius of the dense shell of swept-up ambient material is given by $R = (65.9 \text{ pc}) L_{38}^{0.2} n_0^{-0.2} t_6^{0.6}$, where L_{38} is the mechanical luminosity injected by the starburst in units of $10^{38} \text{ ergs s}^{-1}$, n_0 is the hydrogen number density in units of cubic centimeters, and t_6 the burst age in units of 10^6 yr. Taking $L_{38} = 270$ and $n_0 = 10$ (derived by volume averaging the radial distribution of rms electron density in Mrk 71 given by Kennicutt et al. 1980), we obtain $t_6 = 3.2$ for a displacement of $R = 250$ pc. This age is entirely consistent with the age of 2.5–5 Myr derived by Drissen et al. (2000) in a color-magnitude diagram study of the star cluster NGC 2363-B, to the east of Mrk 71. East is also the direction in which the H I peak is displaced from the optical peak. The second main star cluster in Mrk 71, NGC 2363-A to the west, has an age less than 1 Myr (Drissen et al. 2000) and is too young to have contributed much SN mechanical energy. Thus SN energy input from Mrk 71 appears to be able to account for the displacement between the H I and optical peaks. Clearly, this type of modeling is very approximate as the ISM is very clumpy and the superbubble evolution is not spherical. Moreover, there is not a clear shell structure in the H I map.

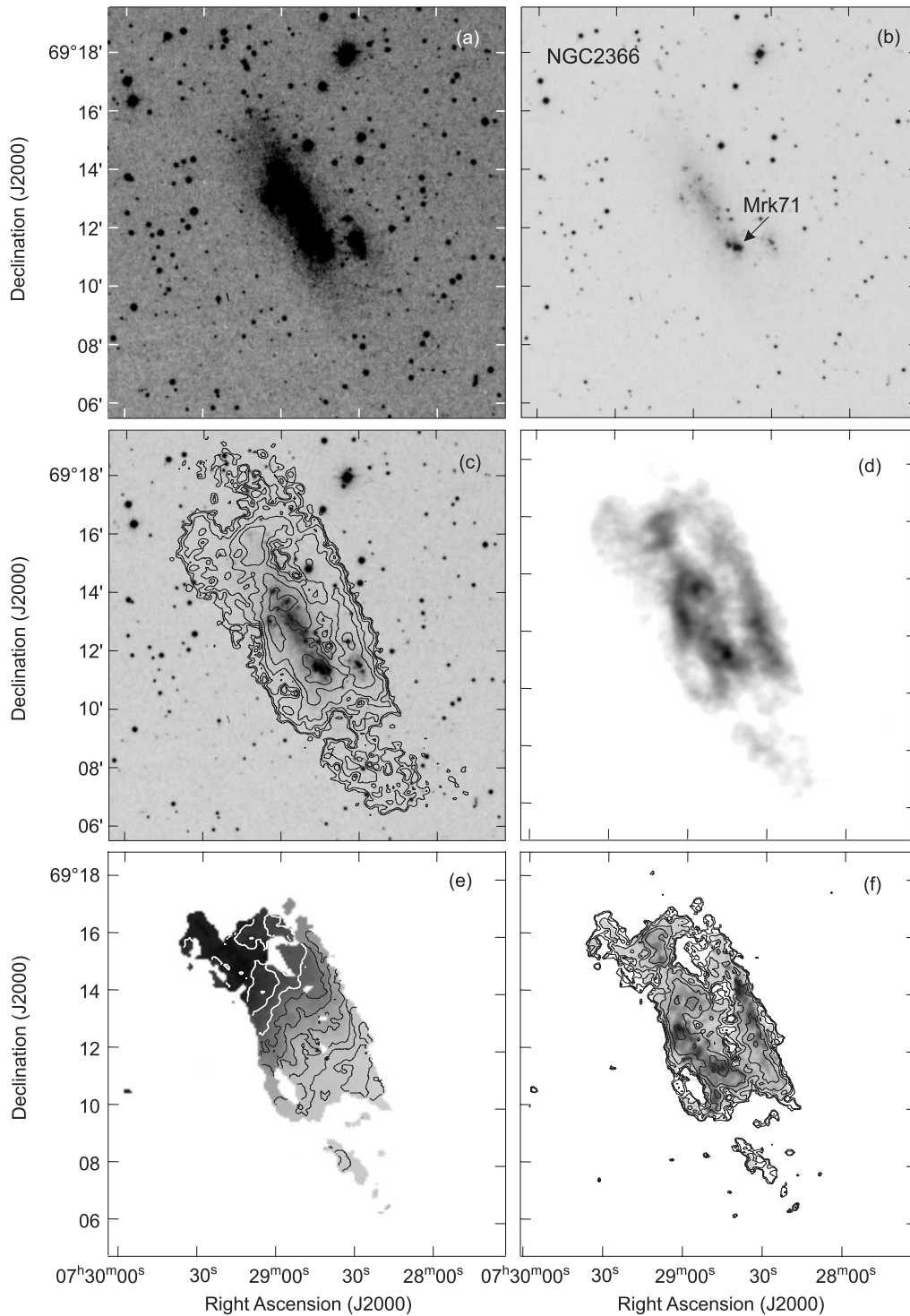


FIG. 1.—NGC 2366 mosaic. The top panels show the DSS image with both (a) a deep and (b) a shallow stretch of the transfer function. The middle panels show the H I distribution, made from the low-resolution data cubes, as (c) contours superposed on the DSS image and (d) gray scales. Contours are drawn at $(1, 2, 4, 8, 16, 32) \times 10^{20} \text{ cm}^{-2}$. Finally, the bottom panels show (e) the moment 1 velocity and (f) moment 2 velocity dispersion maps made from the high-resolution data cubes. Darker shades of gray represent higher velocities, and lighter shades represent lower velocities. The contours on the moment 1 map are isovels (from 45 km s^{-1} in the southwest to 145 km s^{-1} in the northeast in steps of 10 km s^{-1}), while those in the moment 2 map are H I column densities from the high-resolution data drawn at levels of $(1, 2, 4, 8, 16, 32) \times 10^{20} \text{ cm}^{-2}$.

Interestingly, there is a local minimum in the H I distribution on the opposite side (i.e., to the west) of Mrk 71, also supporting the hypothesis that supernova and stellar winds displace the neutral gas. As for the density minima, we interpret them to be cavities carved out in the ISM of the galaxy by SNe and stellar winds from massive stars formed in past

starburst events that have now faded away. The radii of these H I cavities range between $\sim 100\text{--}200 \text{ pc}$, which according to the above expression for R can be obtained, for example, with a set of parameters such as $L_{38} = 10\text{--}100$, $n_0 = 10$, and $t_6 = 3\text{--}6$. The presence of these cavities imply that star formation in NGC 2366 occurs in short bursts (less than

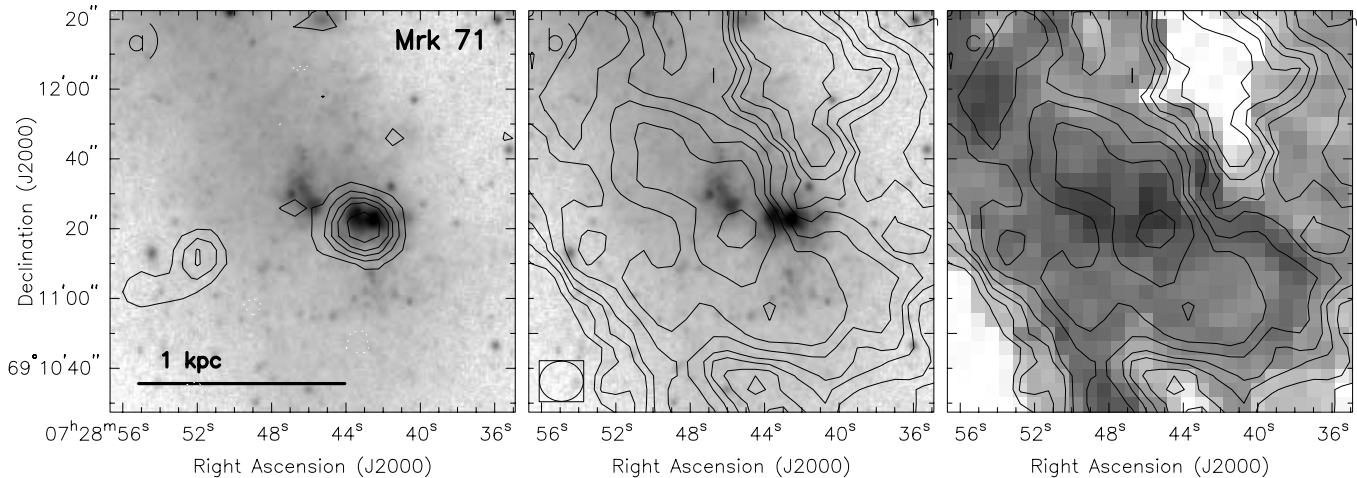


FIG. 2.—Detailed comparison between radio and optical properties in the vicinity of the major star-forming regions in NGC 2366. (a) 1.4 GHz radio continuum emission contours superposed on a gray-scale depiction of the optical CCD image. Contours are drawn at $(-2.5, 2.5, 5, 7.5, 10, 15, 20) \times 1 \sigma$ ($0.37 \text{ mJy beam}^{-1}$). (b) Contours of the integrated H I emission from the high-resolution data superposed on the optical image. Contours are drawn at $(-2.5, 2.5, 5, 7.5, 10, 15, 20, 30, 50) \times 10^{20} \text{ cm}^{-2}$. The boxed ellipse indicates the FWHM beam size for the H I data. (c) The same H I column density contours superposed on a gray-scale representation of the high-resolution H I velocity dispersion map in which the darkest shade corresponds to a dispersion of 13 km s^{-1} .

$\sim 10^7$ yr), with the center of star formation moving about in a stochastic manner in the body of the galaxy.

Another striking feature of the H I intensity map (Fig. 1d) is the presence of two parallel ridges about $6'$ (6 kpc) long running along the major axis of the optical body, separated by a zone nearly devoid of H I. Hunter et al. (2001) interpret these two ridges as a H I ring seen in projection with an inclination angle of 65° . A similar H I ring structure is also seen in the dwarf irregular galaxy Sextans A (Skillman et al. 1988). The center of the ring is not coincident with the center defined by the outer optical isophote (Fig. 1a) but is shifted north along the major axis by $\sim 2'$. The H I ring is surrounded by diffuse neutral gas emission forming a 13.6×4.4 (down to a level of $5 \times 10^{19} \text{ cm}^{-2}$) envelope around the optical body whose size is $5.3 \times 2'$ at the B surface brightness level of 25 mag arcsec $^{-2}$ (Noeske et al. 2000). With an inclination of 65° and assuming NGC 2366 has a flattened structure, this would correspond to a disk with a diameter of ~ 13.6 kpc. The lower resolution observations of Hunter et al. (2001) show low column density H I extending to twice this diameter.

The channel maps for NGC 2366 are shown in Figure 3. We find that the emission peaks are surrounded by a shallow negative “bowl” of emission (*dotted contours*, Fig. 3). These features are an artifact of the deconvolution process that arises when extended emission within the primary beam is not properly measured on the baselines sampled. Our VLA flux represents only 67% of the single-dish measurement of TM81 (Fig. 6a). This is confirmed by examination of the channel maps of Hunter et al. (2001), who used the more compact VLA D configuration, which better samples this extended emission. Hunter et al. recover a total H I mass of $8.0 \times 10^8 M_\odot$, as compared to our VLA value of $4.1 \times 10^8 M_\odot$. Contrary to what is stated in their paper, Hunter et al.’s measurement is in agreement, within the errors, with the single-dish measurement of TM81. It also agrees with those of Huchtmeier et al. (1981), Wevers et al. (1986), and Swaters (1999).

3.2.2. H I Kinematics

The H I kinematics of NGC 2366 are displayed in the moment 1 and moment 2 maps in the bottom row of Figure 1 and

in the channel maps in Figure 3. These figures show a general southwest to northeast kinematic gradient in NGC 2366, indicative of rotation. Since the kinematics seem to be approximately rotational, we have some confidence in the parameters derived by the tilted-ring fit to the first-moment map.

The rotation curve resulting from the fit to the velocity field of NGC 2366 is shown in Figure 4. The solid line is the model curve, and the open circles represent the deprojected rotational velocity computed from the first moments and the geometrical parameters. The parameters for the outermost ring of the best fit are an inclination angle of $i = 59^\circ$, a position angle of $\text{PA} = 51^\circ$, and a systemic velocity of 101 km s^{-1} . TM81 give the heliocentric velocity as $96 \pm 5 \text{ km s}^{-1}$. Hunter et al. (2001) also fitted their velocity field with a Brandt (1960) function and tilted-ring models. Their adopted systemic velocity is $99.1 \pm 0.2 \text{ km s}^{-1}$, with an inclination of $i = 65^\circ$ and position angle of $\text{PA} = 46^\circ$. Wevers et al. (1986) find values of $i = 65^\circ$ and $\text{PA} = 40^\circ$, and Swaters (1999) find $i = 59^\circ$ and $\text{PA} = 42^\circ$. These values are all in rough agreement with our fit. The rotation curve derived by Hunter et al. (2001) rises linearly with radius for $r \lesssim 110''$, characteristic of solid-body rotation, and then flattens out at a rotational velocity of $\sim 47 \text{ km s}^{-1}$. Our derived rotation curve (Fig. 4) shows a similar behavior except that the rotation speed is higher, $\sim 60 \text{ km s}^{-1}$. Our higher value is the same as that derived by Swaters (1999) at his last measured radius of 5.9 , which is also our last measured point. The rotation curve of Hunter et al. (2001) extends out to a radius of $\sim 10'$. They find that beyond a radius of 5.7 , the rotation curve remains flat for the approaching side, while it begins to decline for the receding side.

However, the velocity field is not purely rotational. The isovelocity contours in Figure 1e show a number of kinks and bends, and the individual channel maps show features with an S shape, as opposed to the classical V shape observed in regularly rotating spiral galaxies (see e.g., Bosma 1981). Such departures are often attributed to streaming motions due to the presence of a bar or a strong spiral shock, or to a warp in the H I disk. The presence of a bar is unlikely in NGC 2366, as detailed surface photometry (Noeske et al. 2000) show no evidence for it, despite its classification as a barred Magellanic-type dwarf

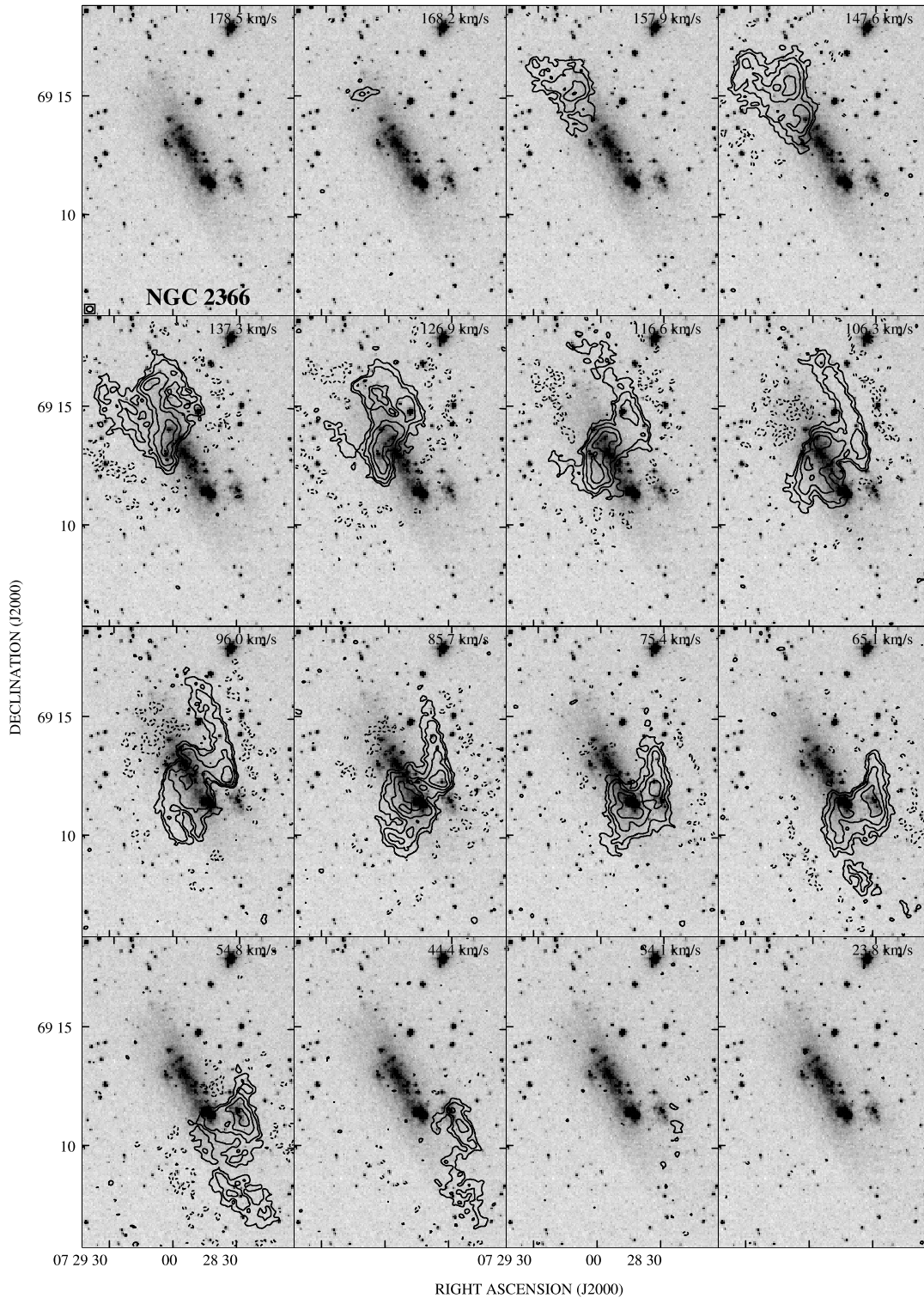


FIG. 3.—NGC 2366 H I channel map contours superposed on a gray-scale representation of the optical DSS image. The low-resolution data cube is used, with the resolution indicated in the lower left corner of the first panel (*top left*). Only channels showing emission are plotted. The channel spacing is 10.3 km s^{-1} , and the heliocentric velocity of each channel is printed in the upper right corner of each panel. Contours are drawn at $(-3, 3, 6, 12, 24) \times 1 \sigma$, where $1 \sigma = 0.78 \text{ mJy beam}^{-1} = 3.7 \times 10^{19} \text{ cm}^{-2}$.

irregular galaxy. There is also no evidence for spiral structure in NGC 2366. Many of the isovelocity kinks correspond to ridges of high dispersion, as shown in Figure 1*f*. These ridges have velocity dispersions of $9\text{--}15 \text{ km s}^{-1}$, compared with a mean velocity dispersion of $\sigma = 7.7 \text{ km s}^{-1}$. The ratio V_{rot}/σ of the rotational velocity to the velocity dispersion is equal to 8.7

(Table 3). A detailed examination shows that the H I line profiles are double-valued in many of the regions of high velocity dispersion. We illustrate this in Figure 5, which shows a matrix of individual spectra. Double profiles, indicated by asterisks, can be seen in the upper right and lower center of this plot. These double profiles suggest there may be multiple

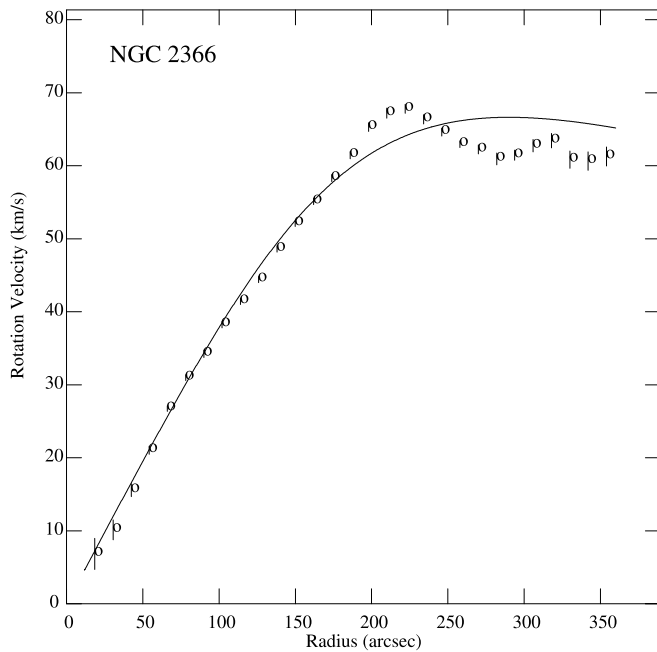


FIG. 4.—NGC 2366 rotation curve. The solid line is the model curve, and the open circles represent the deprojected rotational velocity computed from the first moments and the geometrical parameters.

kinematic components present in NGC 2366. We discuss this issue in more depth in § 3.2.3. Because of these motions, the rotational model derived above should be considered very approximate.

There are other regions of anomalous H I kinematics in NGC 2366. In particular, there are regions of high velocity dispersion in the vicinity of Mrk 71. This is seen in more detail in Figure 2c. This panel shows that the H I velocity widths increase in the region of highest column density located to the east of the giant H II region. This indicates that the gas is being stirred up by the mechanical input of energy from the starburst, as discussed before. Unlike the high-dispersion regions mentioned above, the line profiles at this location are not double valued (Fig. 5). This is somewhat surprising, since Roy et al. (1991) found double-peaked profiles in the [O III] emission lines in the region of Mrk 71, indicative of an expanding bubble of ionized gas. The [O III] lines were split by 90 km s^{-1} , well within our capability to resolve, given our kinematic resolution of 10 km s^{-1} . This may indicate that the bubble is fully ionized or that the neutral gas in the bubble has been blown out.

3.2.3. H I Gas and Star Formation

The double-peaked line profiles mentioned above suggest multiple gaseous components in NGC 2366. Other suggestions of multiple components come from a comparison of our high-resolution maps with the lower resolution, higher surface-brightness sensitivity VLA C+D configuration observations of Hunter et al. (2001). Specifically, Hunter et al. measure a velocity dispersion of $12\text{--}20 \text{ km s}^{-1}$ within the optical disk from their low-resolution C+D configuration map ($34'' \times 29''$ FWHM), while both we and they measure a mean dispersion of $5\text{--}10 \text{ km s}^{-1}$ within the optical disk from the C configuration data alone. Moreover, Hunter et al. find an even higher characteristic dispersion ($20\text{--}30 \text{ km s}^{-1}$) outside of the optical disk, which they attribute to long-range turbulence. As support for

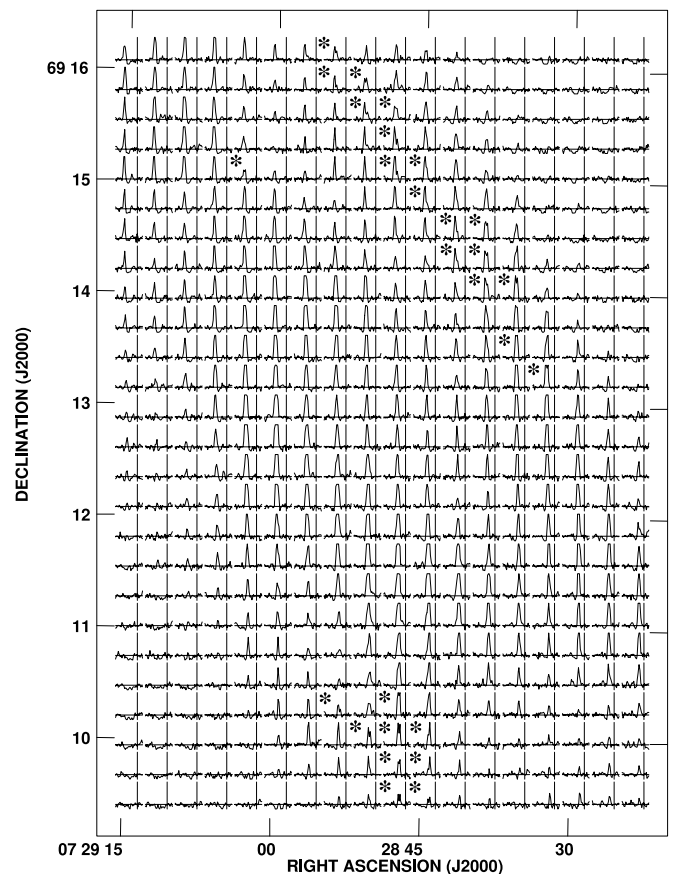


FIG. 5.—Grid of individual H I line profiles for NGC 2366. The line profile intensities are plotted from -2 to 10 mJy beam^{-1} . Channels are plotted along the x-axis, with corresponding velocities ranging from $+251 \text{ km s}^{-1}$ on the left to -59 km s^{-1} on the right. Double-peaked profiles are indicated by asterisks.

this idea, they cite the tendency for regions of high dispersion to be associated with regions of lower H I column density.

We adopt here another point of view. We believe these observations can be understood in terms of the standard model of the interstellar medium (ISM), in which there are predominantly two phases of neutral hydrogen in approximate pressure balance: the cold neutral medium (CNM) and the warm neutral medium (WNM) (e.g., McKee & Ostriker 1977; Wolfire et al. 1995; Heiles & Troland 2003; Young et al. 2003). In this picture, the CNM has a relatively small scale height and velocity dispersion. The WNM is warmer and more diffuse, with a larger scale height and velocity dispersion. In external galaxies, the CNM is associated primarily with the optical disk, and the relative contribution from the WNM increases with radius (Braun 1995, 1997). We suggest that our C configuration observations mostly resolve out the more extended warmer component and emphasize the cooler disk component. The lower resolution observations of Hunter et al. measure a larger fraction of the low surface brightness flux from the broader warm component and therefore measure larger line widths. In this interpretation, the increase in the velocity dispersion outside the optical disk would be due to the lack of a cold component. Similarly, the anticorrelation between high velocity dispersion and low H I column density reported by Hunter et al. would be a reflection of the lack of the denser cold component, rather than an increase in the kinetic motions of the warm component. Young et al. (2003) explicitly detected these two components in their H I observations

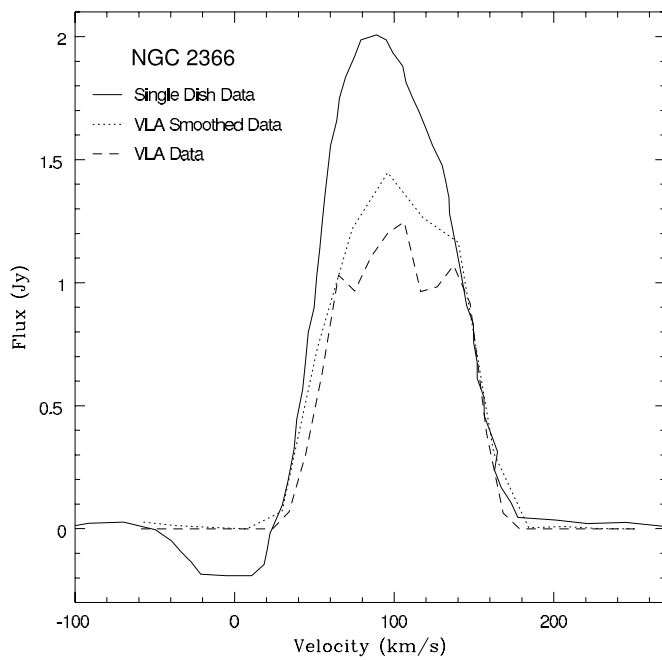


FIG. 6a

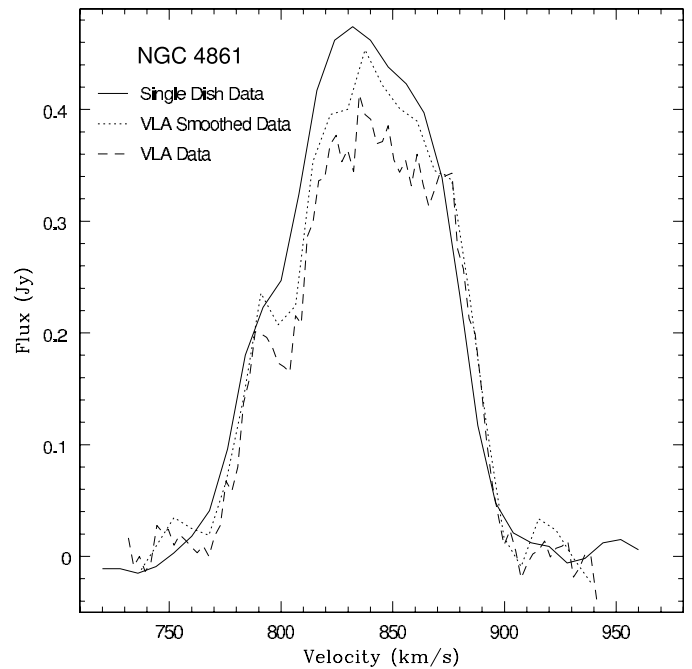


FIG. 6b

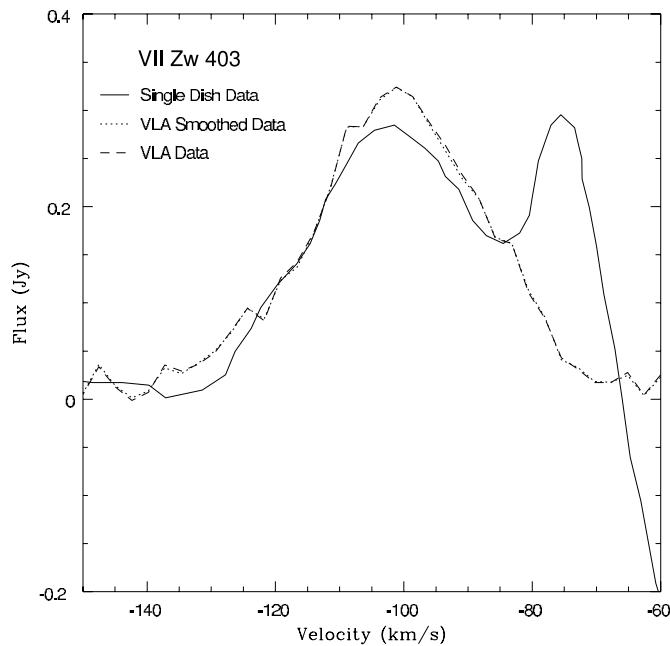


FIG. 6c

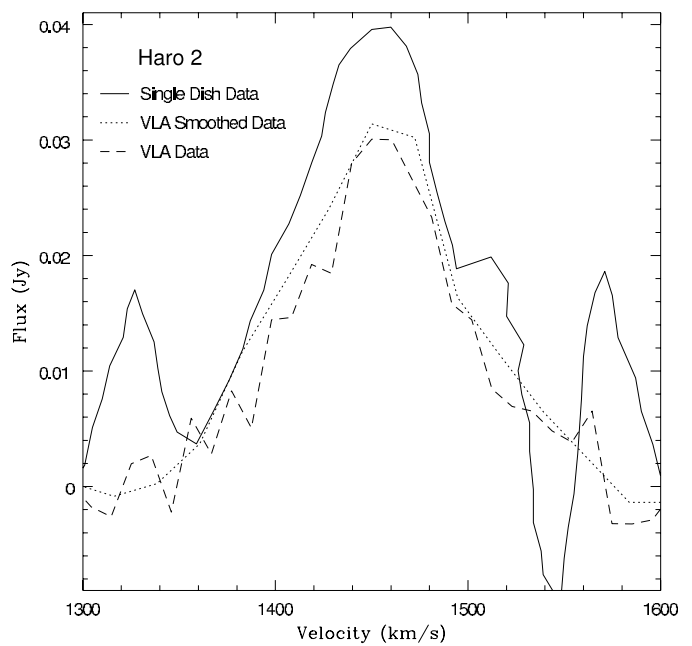


FIG. 6d

FIG. 6.—Comparison of the H I spectra from the VLA smoothed data (*short dashed lines*) and low-resolution data (*long dashed lines*) with uncorrected single-dish spectra from TM81 for NGC 2366, VII Zw 403, and Haro 2, and with an uncorrected new single-dish spectra for NGC 4861 (*solid lines*). Clockwise from the upper left are spectra for NGC 2366, NGC 4861, VII Zw 403, and Haro 2.

of four dwarf irregular galaxies (see also the discussion concerning Fig. 13 for NGC 4861 in § 3.3.3).

Taking our observations and those of Hunter et al. together, we derive a picture in which there is an extended envelope of warm gas in NGC 2366, which contributes significantly even within the optical body of NGC 2366. In addition, there is a cooler denser component directly associated with the disk. The disk gas should be primarily supported by rotation, but the H I envelope may have slightly different kinematics. Similar components with different kinematics have been inferred from H I observations and detailed modeling of several nearby galaxies (e.g., Fraternali et al. 2002; Swaters et al. 1997).

Some of the kinematic anomalies mentioned above (kinks in the velocity field, double-peaked line profiles) may be due to these two disk and envelope components.

3.2.4. Radio Continuum

We have also made continuum maps of the field containing NGC 2366. No significant disk emission is seen. A major fraction of the continuum emission comes from the supergiant H II region Mrk 71. There is also some continuum emission associated with the H II region to the east of Mrk 71. Their respective 1.4 GHz fluxes are 8.1 and 3.6 mJy. A blow-up of this region is shown in Figure 2a. Our 21 cm continuum flux

for Mrk 71 is very similar to the 6.3 cm flux of 10 ± 1 mJy and the 2.8 cm flux of 11 ± 1 mJy obtained with the Effelsberg 100 m radio telescope (Klein et al. 1984), giving a spectral index of ~ 0 . Thus the radiation from Mrk 71 is purely thermal, from free-free emission of the ionized gas. This means that the stellar population in Mrk 71 is extremely young, as massive stars have not had time to die and give birth to a supernova population, the radio continuum emission of which has a considerably steeper slope. The very young ages of, respectively, less than 1 and 2.5–5 Myr are indeed derived for the two main super star clusters NGC 2363-A and NGC 2363-B in Mrk 71, where most of the radio continuum comes from (Drissen et al. 2000). As for the cluster to the east of Mrk 71, those authors derive an age of 10 Myr.

In summary, the H I distribution of NGC 2366 is very clumpy, with many peaks and valleys. It shows two parallel ridges of H I, which, deprojected, may be part of a H I ring. There is an overall rotation of the H I disk of gas, although many velocity kinks are present, which may indicate multiple kinematic components. The velocity dispersion inferred from the second-moment map increases with radius, leading us to suggest that there is an extended envelope of warmer gas in addition to a disk of cooler H I gas. The zones of high star formation are invariably associated with regions of high H I column densities, although the reverse is not true.

3.3. NGC 4861 and Mrk 59

Like NGC 2366, NGC 4861 belongs to the class of cometary BCDs as defined by Loose & Thuan (1985). Arp (1966) describes NGC 4861 (a.k.a. Arp 266) in his Atlas of Peculiar Galaxies as “an object with irregular clumps, resolved into knots with a very bright knot (diameter = 1 kpc) at the southeastern end.” The knots are in fact a chain of H II regions, resulting from propagating star formation along the galaxy’s elongated body and ending with the high surface brightness supergiant H II region Mrk 59 \equiv I Zw 49 at its southeastern end.

Thuan et al. (1987) have obtained H α Fabry-Pérot maps of NGC 4861. They found that Mrk 59 is ~ 50 times brighter in H α than any other feature in NGC 4861. The supergiant H II region is surrounded by loops and filaments, with large holes in the H α distribution (their diameters vary between ~ 75 –420 pc), suggestive of past supernova events. There is a chain of 14 fainter and smaller H II regions across NGC 4861, suggesting self-propagating star formation. All H II regions are embedded in much fainter diffuse H α emission. The H α velocity field shows a northeast-southwest gradient, which can be understood as the rotation of an inclined disk, with the bright end approaching and the faint end receding. On this overall regularity in the velocity on large scales are superimposed irregularities on smaller scales. Detailed examination of the line profiles in Mrk 59 shows that they are double-peaked, suggestive of an expanding bubble of ionized gas, as in Mrk 71.

Dinerstein & Shields (1986) first detected broad Wolf-Rayet stellar features in Mrk 59 indicating the presence of late nitrogen and early carbon Wolf-Rayet stars. Guseva et al. (2000), using the spectroscopic observations of Izotov et al. (1997), found that several dozens of Wolf-Rayet stars are present. Noeske et al. (2000) used deep ground-based spectrophotometric observations of the supergiant H II region to derive an oxygen abundance $12 + \log(\text{O}/\text{H}) = 8.011 \pm 0.003(Z_{\odot}/8)$, typical of BCDs. O abundances were also derived for two other emission knots along the elongated body and were found to be

the same within the errors. The small scatter in metallicity along the major axis of Mrk 59 (~ 0.2 dex) suggests that the mixing of elements in the ionized gas has been efficient on a spatial scale of several kiloparsecs.

Spectral population synthesis in combination with color-magnitude diagrams and color profiles give a most probable age of ~ 2 Gyr for the LSB elongated body, with an upper limit of ~ 4 Gyr (Noeske et al. 2000). As with NGC 2366, this age is considerably smaller than the typical age (5 Gyr or greater) of the underlying stellar population in BCDs of other types. Cometary galaxies as a class appear to be relatively young galaxies. Thuan et al. (2002) have used the *Far Ultraviolet Spectroscopic Explorer* (FUSE) to study the abundances in the ISM of NGC 4861 from UV absorption lines. They found that the heavy-element abundance in the neutral gas of NGC 4861 is about a factor of 10 less than that of the BCD Mrk 59, or about 1.2% of the solar abundance. This also supports the idea that NGC 4861 is relatively young.

We discuss in the following the H I properties of Mrk 59 and compare our results with those of Wilcots et al. (1996) obtained at a lower spatial resolution with the more compact VLA D configuration. At the distance of 10.7 Mpc, $1''$ in Mrk 59 corresponds to 52 pc.

3.3.1. H I Morphology

Like NGC 2366 (and other dwarf galaxies), the H I extent (6.8×4.6 at the column density $N(\text{H I}) = 5 \times 10^{19} \text{ cm}^{-2}$ or $21.1 \text{ kpc} \times 14.3 \text{ kpc}$) is larger than the optical extent (2.3×1.0 at the B isophotal level of 25 mag arcsec $^{-2}$, or $8.1 \text{ kpc} \times 3.1 \text{ kpc}$). Assuming that the H I gas is distributed in a thin disk, then its axial ratio gives an inclination angle of 65° , in good agreement with the value of 67° derived by Wilcots et al. (1996) and in this paper from the H I kinematics (§ 3.3.2).

The total H I emission map for NGC 4861, shown in Figures 7d and 8, reveals a very clumpy ISM, not unlike that of NGC 2366. Because NGC 4861 is 3.1 times more distant, H I minima are not as evident as in NGC 2366. The observations of Wilcots et al. (1996) revealed a low column density envelope of H I extending toward an H I companion located 6.2 (19.3 kpc) to the east. We also detect this envelope by smoothing our data to a $35''$ resolution. The resulting H I distribution is shown superposed on an optical CCD image obtained by Noeske et al. (2000) in Figure 9. The H I cloud has no optical counterpart on the optical CCD image or the DSS and appears similar to the H I companions seen by Taylor et al. (1994) near other BCDs. The H I envelope of NGC 4861 shows an extended feature pointing toward the H I companion, suggesting some type of interaction between the two.

We recover a total H I flux for the NGC 4861 system (including the envelope and companion) of $\simeq 1.1 \times 10^9 M_{\odot}$. This is similar to that found by Wilcots et al. (1996) after accounting for their adopted distance of 9 Mpc. This also agrees within the errors with the new corrected single-dish flux obtained with the 140 foot (43 m) telescope (see Table 1 and Fig. 6b). The mass of neutral gas in NGC 4861 is twice as large as in NGC 2366. Of the total mass, we associate an H I mass of $M_e \simeq 1.3 \times 10^7 M_{\odot}$ with the H I companion and $M_e \simeq 1.1 \times 10^8 M_{\odot}$ for the H I envelope.

As in NGC 2366, we see in NGC 4861 a close correspondence between the regions of active star formation and the H I column density peaks (see Figs. 6c and 6d). The H I intensity map (Fig. 7d) shows four H I peaks roughly aligned along the major axis of the optical body of NGC 4861 (delineated by the highest contour in Fig. 7c, drawn at a column density of

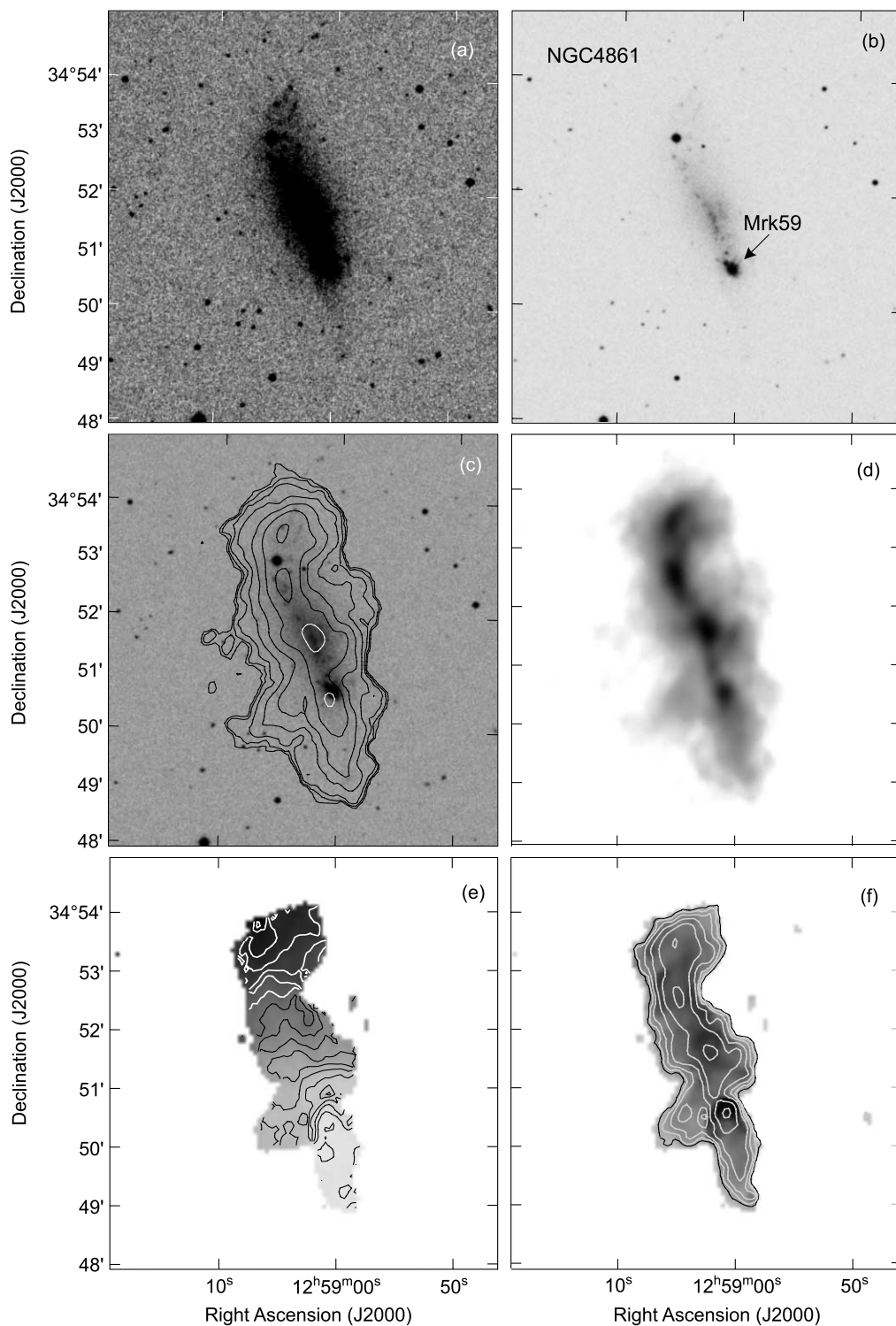


FIG. 7.—NGC 4861 mosaic. Same layout as in Fig. 1. Contour levels for the low-resolution H I data are $(0.5, 1, 2, 4, 8, 16, 32) \times 10^{20} \text{ cm}^{-2}$, while contours for the high-resolution data are a factor of 2 higher. The isovelocity contours on the moment 1 map are drawn from 790 km s^{-1} in the south to 880 km s^{-1} in the north in steps of 10 km s^{-1} .

$3.2 \times 10^{20} \text{ cm}^{-2}$). Mrk 59 is at the location of the southernmost H I peak. The middle peak coincides with the center of NGC 4861, and there are two regions north of this. While there are young stars associated with the last two peaks, star formation activity is much less there. So in general, there is a good correlation between peaks in the neutral gas and star formation.

The smaller scale association between the atomic gas and starlight is shown in Figure 8*b*. This figure shows a blow-up of

the area around the supergiant H II region Mrk 59. Again, as is the case of Mrk 71, the peak in the H I column density is displaced by about 500 pc to the south of Mrk 59, and there is a local minimum in the H I distribution in the opposite direction, again suggesting the sweeping or ionization of neutral gas within the bubble by young stars and supernovae. In the same manner as for NGC 2366 and with all the caveats attached to such a model, we can estimate the mechanical

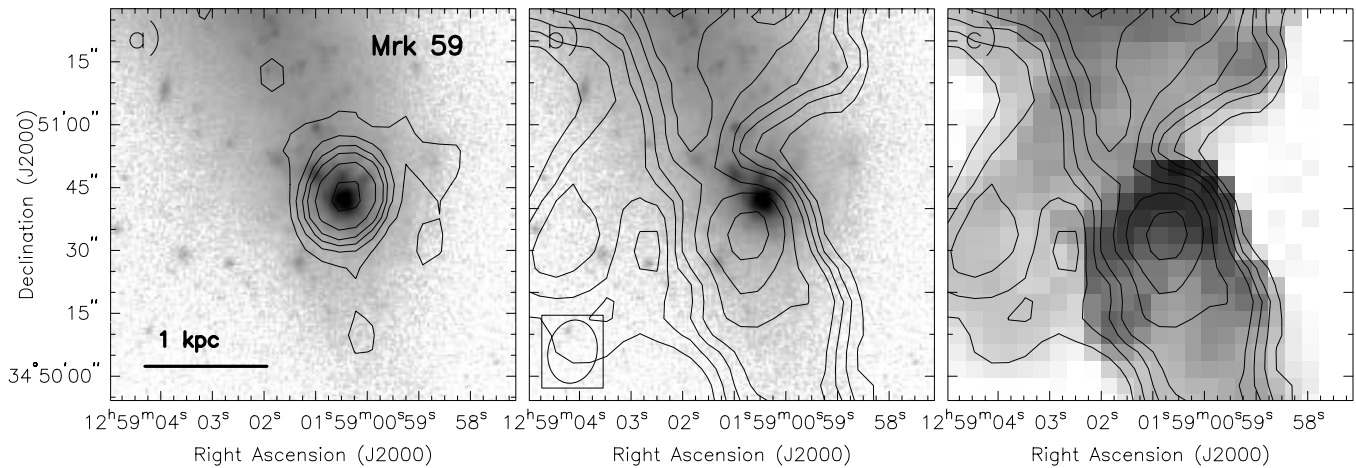


FIG. 8.—Detailed comparison between radio and optical properties in the vicinity of the major star forming regions in NGC 4861. (a) 1.4 GHz radio continuum emission contours superposed on a gray-scale depiction of the optical CCD image. Contours are drawn at $(-2.5, 2.5, 5, 7.5, 10, 15, 20) \times 1 \sigma$ ($0.25 \text{ mJy beam}^{-1}$). (b) Contours of the integrated H I emission from the high-resolution data superposed on the optical image. Contours are drawn at $(-2.5, 2.5, 5, 7.5, 10, 15, 20, 30) \times 10^{20} \text{ cm}^{-2}$. The boxed ellipse indicates the FWHM beam size for the H I data. (c) The same H I column density contours superposed on a gray-scale representation of the high-resolution H I dispersion map in which the darkest shade corresponds to a dispersion of 19 km s^{-1} .

energy injected by SNe in the ISM of NGC 4861. Adopting a stellar upper mass limit of $100 M_{\odot}$ and a Salpeter IMF, Calzetti (1997) gives a SN rate of 0.005 yr^{-1} for NGC 4861, which corresponds to a mechanical energy input of $1.6 \times 10^{41} \text{ ergs s}^{-1}$, assuming a kinetic energy input of 10^{51} ergs per SN. Adopting the expression given in § 3.2.1 for the time evolution of a H I shell and an average ambient density n_0 of 10 cm^{-3} , we obtain a displacement of 500 pc after a time

of $\sim 5 \text{ Myr}$, which agrees well with the age of 4.5 Myr derived by Barth et al. (1994) for the brightest star cluster in NGC 4861.

3.3.2. H I Kinematics

The H I kinematics of NGC 4861 are illustrated by the isovelocity (*left*) and velocity dispersion (*right*) contour maps in the bottom row of Figure 7 and by the low-resolution

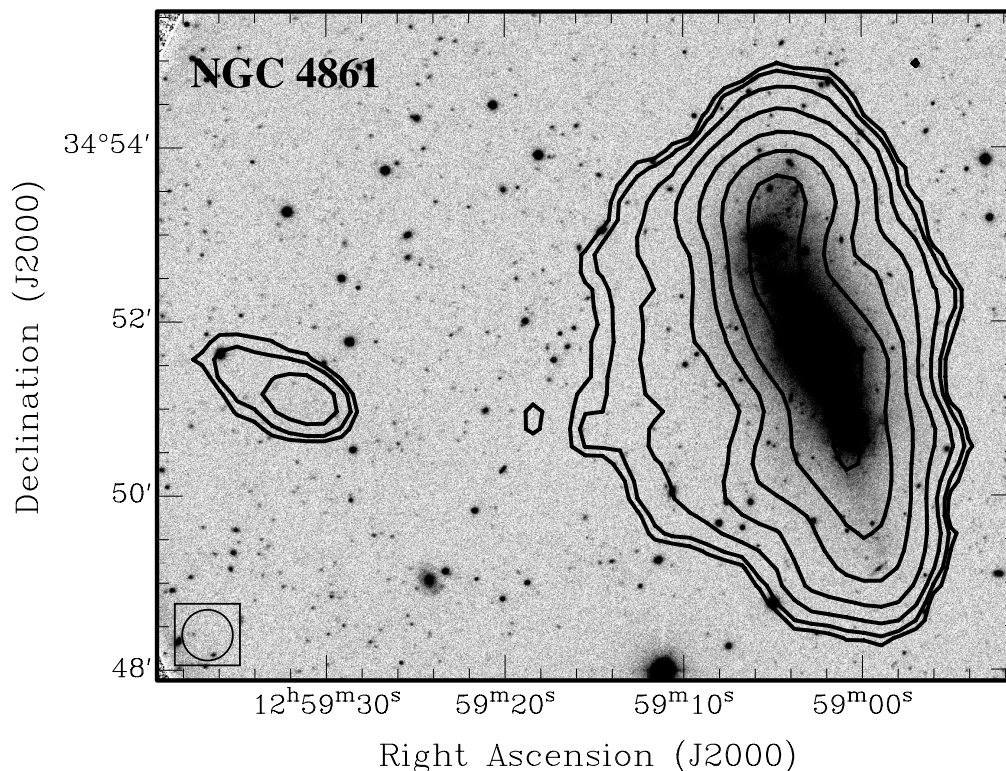


FIG. 9.—Extended gas distribution in NGC 4861. Gray scales represent the optical CCD data, while contours show the H I column density from the low-resolution moment map convolved to a $35''$ resolution. Contours are drawn at $(1, 2, 4, 8, 16, 32, 64) \times 33.3 \text{ mJy beam}^{-1} \text{ km s}^{-1}$, where the lowest contour corresponds to a column density of $3 \times 10^{19} \text{ cm}^{-2}$. This image shows the extended H I envelope of NGC 4861 and the H I cloud lying directly to the east at a projected separation of 19 kpc. There is no visible optical counterpart to the H I cloud.

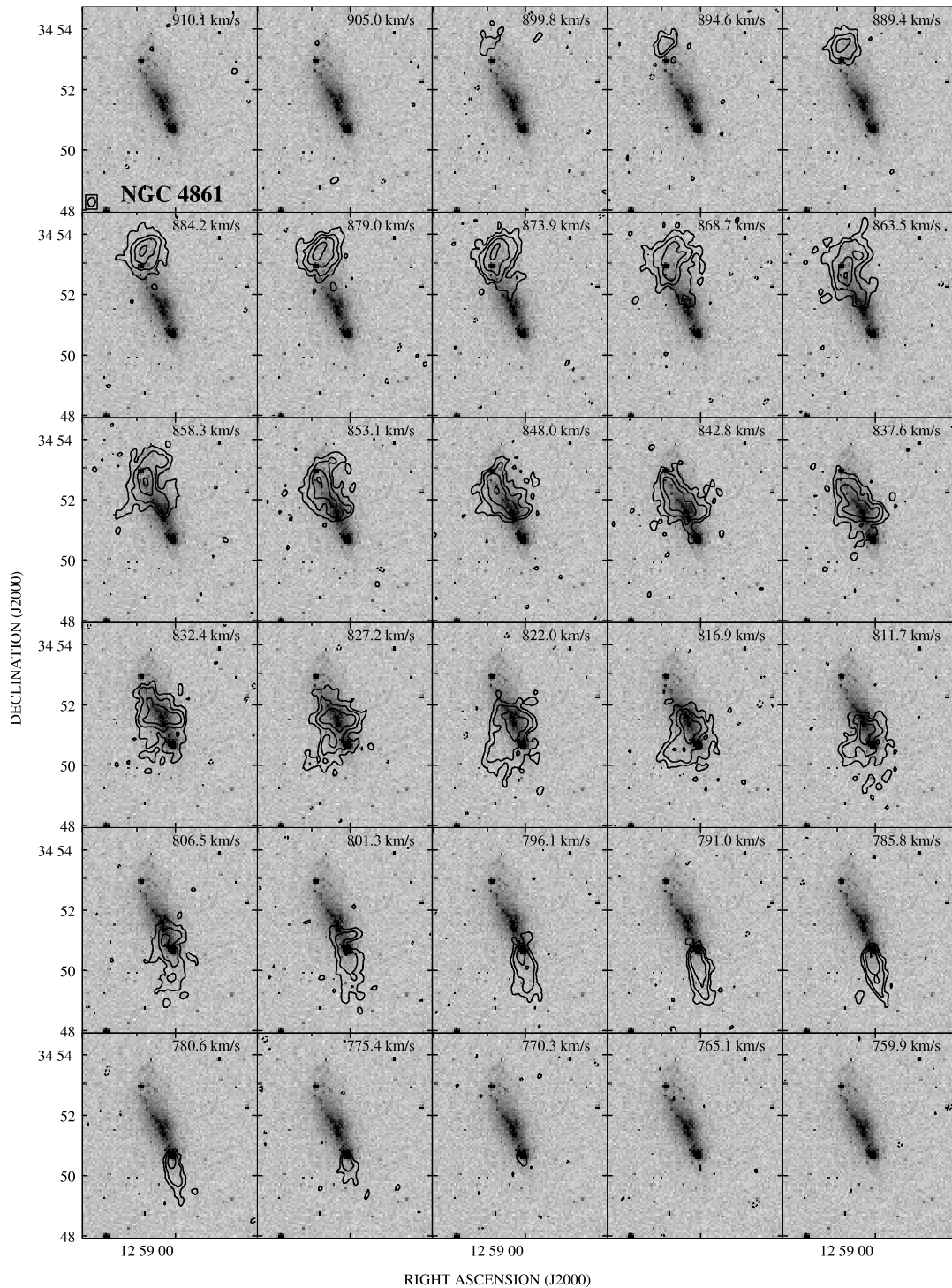


FIG. 10.—Low-resolution H I channel map contours of NGC 4861 superposed on a gray-scale representation of the optical DSS image. The resolution is indicated in the lower left corner of the first panel (*top left*). The channel spacing is 5.2 km s^{-1} , and contours are drawn at $(-3, 3, 6, 12, 24) \times 1 \sigma$, where $1 \sigma = 1.1 \text{ mJy beam}^{-1} = 1.1 \times 10^{19} \text{ cm}^{-2}$.

and smoothed channel maps in Figures 10 and 11. As in NGC 2366, the channel maps show a southwest-northeast kinematic gradient, characteristic of a highly inclined rotating disk. NGC 4861 has been classified as a barred Magellanic-type dwarf irregular just like NGC 2366. But, as in the case of NGC 2366, although the H I envelope of NGC 4861 is elongated in the southwest-northeast direction, we do not believe it is a barlike structure because optical surface photometry does not show any evidence for the presence of a bar

(Noeske et al. 2000). There is also no evidence for it in the H I kinematics.

The rotation curve resulting from the fit to the velocity field of NGC 4861 is shown in Figure 12. The solid line represents the model and the open circles the deprojected rotational velocities. The parameters for the outermost ring of the best fit are an inclination angle of 82° , a position angle of 17° , and a systemic velocity of 830 km s^{-1} . This is somewhat lower than the heliocentric velocity of 905 km s^{-1} given by TM81 from their

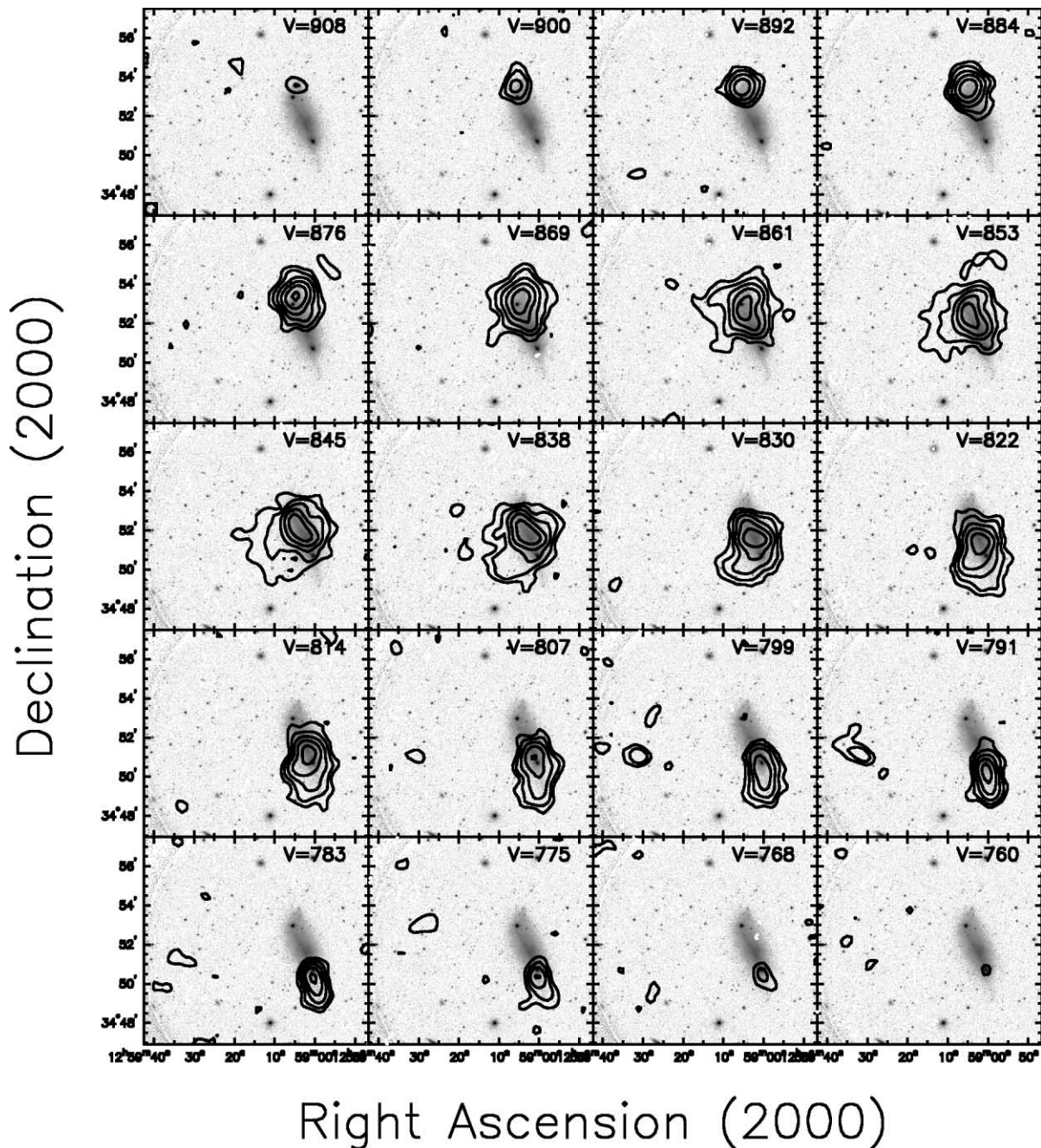


FIG. 11.—Channel map contours from the smoothed data cube of NGC 4861 (resolution = $35''$) superposed on a gray-scale representation of the optical DSS image. The resolution is indicated in the bottom left corner of the first panel (*top left*). The channel spacing is 7.8 km s^{-1} , with the heliocentric velocity of the channel printed in the top right corner of each panel. Contours are drawn at $(-3, 3, 6, 12, 24, 48) \times 1 \sigma$, where $1 \sigma = 0.9 \text{ mJy beam}^{-1} = 6.3 \times 10^{18} \text{ cm}^{-2}$.

300 foot (91 m) telescope single-dish profile. To resolve the discrepancy, we reobserved NGC 4861 with the NRAO 140 foot (43 m) telescope in 1992 March. The new profile gives a heliocentric velocity of $833 \pm 5 \text{ km s}^{-1}$, in good agreement with the VLA value. Evidently, the TM81 value is too high. The rotation curve shows a solid-body behavior for radii $\lesssim 90''$ and continues to increase out to our last observed point at radius $150''$ and $v = 52 \text{ km s}^{-1}$. Our maximum velocity is considerably lower than the value of 80 km s^{-1} inferred by Wilcots et al. (1996). The kinematical center appears to coincide with the center as defined by the outermost optical isophotes.

As in NGC 2366, the velocity field of NGC 4861 is not purely rotational and shows a number of irregularities. However the individual channel maps (Figs. 10 and 11) do not

show the S shape seen in NGC 2366, implying no strong streaming motions. The H I line profiles do not show the multi-peaked values seen in NGC 2366, implying that the H I disk has no significant warp. At the location of Mrk 59, the H I profiles do not show the double-peaked structure seen in the H α profiles. As in Mrk 71, this is probably an indication that the bubble is fully ionized or that the neutral gas in the bubble has been blown out.

3.3.3. H I Velocity Dispersions

The mean H I velocity dispersion is $\sigma = 8.4 \text{ km s}^{-1}$. This corresponds to a V_{rot}/σ ratio of 6.4 (Table 3). The largest value of $\sim 20 \text{ km s}^{-1}$ is associated with the supergiant H II region Mrk 59 (Fig. 8). As in NGC 2366, there appears to be

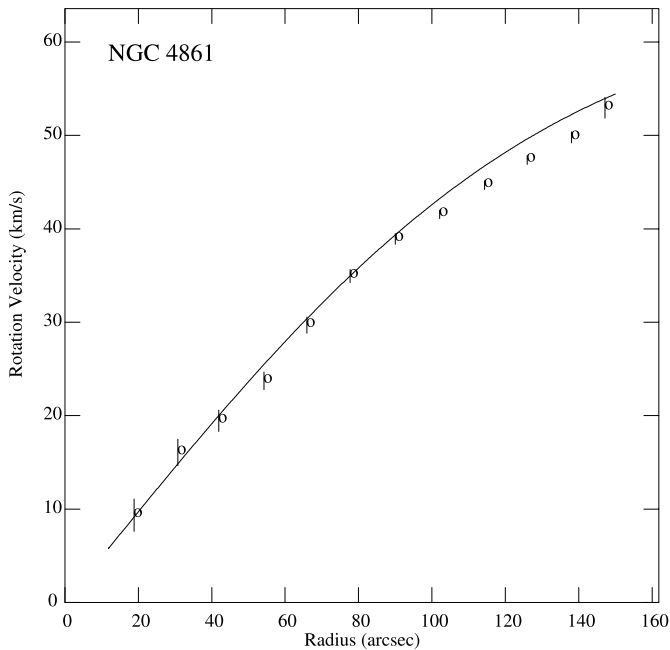


FIG. 12.—NGC 4861 rotation curve. The solid line is the model curve, and the open circles represent the deprojected rotational velocity computed from the first moments and the geometrical parameters.

regions of high H I velocity dispersion in the range 10–20 km s⁻¹ in which there are no obvious optical features. We can study in more detail this H I/optical anticorrelation by considering a major axis “position-velocity profile”: a plot of H I line intensity as a function of velocity and position along the major axis. This profile is presented in Figure 13, with contours drawn at (3, 6, 9) times the rms noise level. The left panel shows the H I velocity dispersion map with the location of the extracted position-velocity plot delineated by a thin dashed rectangle. The moment map has been rotated 19° clockwise to align the major axis north-south. The resulting position-velocity intensity profile is shown in the right panel. The small square boxes delineate various regions discussed below.

We first note that the region of highest H I velocity dispersion (sight line “d” in Fig. 13) corresponds to an abrupt break in the position-velocity profile. There is a discontinuity from the linearly increasing velocity behavior in the north to a constant velocity behavior in the south, and a clear gap between the two regimes. The broad region in the velocity dispersion map reflects the broad velocity spread of the low-level emission bounding both north and south regions. It seems likely that this apparent kinematic increase would be considerably reduced if there was denser gas in this region. The impression is that there is missing atomic gas right at the location of the supergiant H II region, possibly as a consequence of blowout. The position-velocity profile would appear much more regular if the dense region just below sight line “d” in Figure 13 would be moved into the gap. We suggest that this gas has been moved away from the vicinity of Mrk 59 by the action of stellar winds and SNe and has been accelerated toward us, changing its line-of-sight velocity from ~805–785 km s⁻¹. The energetic requirements for such a change in velocity are not unreasonable. The mass of the displaced gas being $2 \times 10^6 M_{\odot}$, the energy required is 8×10^{51} ergs, or that of 8 SNe. With a SN rate of 0.005 yr⁻¹, this would require a time of only 1600 yr.

The position-velocity profile of NGC 4861 (Fig. 13) serves to illustrate some issues raised in the discussion of NGC 2366 concerning the presence of a cold and warm neutral medium. In the left panel of Figure 13 we have indicated three boxes, labeled *a*, *b*, and *c*, each of width 20'' (corresponding to the area of two beams), over which we have summed spectra in order to improve the signal-to-noise ratio and fit Gaussians to the line profiles. Region *a* was selected to correspond to a region with a local H I column density peak and a low velocity dispersion as judged from the moment 2 map (FWHM = 20 km s⁻¹), region *b* was selected to have a local H I column density peak and an intermediate velocity dispersion (FWHM = 26 km s⁻¹), and region *c* was selected to correspond to a region with a local H I column density minimum and a large velocity dispersion (FWHM = 32 km s⁻¹). The resulting profiles extracted from these regions are shown in Figs. 14–16. Gaussians were fitted interactively using the *imageprofilefitter* tool in AIPS++. In the top panels we show the result of fitting a single Gaussian component to the spectra, while in the bottom panels we show the result for fitting double Gaussians. The residuals to the single Gaussian fits to spectra *a* and *b* are decidedly different from the noise in the line-free channels at lower velocities. In all cases, χ^2 tests prefer the double-Gaussian fits, although only marginally so for region *c*. For the regions extracted from local H I maxima (*a* and *b*), the fits prefer a narrow (FWHM ~ 15 km s⁻¹) and a broader (FWHM ~ 30 km s⁻¹) component, while in region *c* both components are broad.

These results support our interpretation that the H I gas has two components, one cooler and one warmer. Young et al. (2003) found similar evidence for this multiphase structure in their much more extensive analysis of high-quality H I spectra in four dwarf irregular galaxies. They found that the warm component was ubiquitous, whereas the cold component was less extensive and mostly associated with higher H I column densities. The position-velocity plot (Fig. 13) suggests a similar situation in NGC 4861: specifically, we note that the regions with denser H I concentrations (e.g., regions *a* and *b*; also note the region just below sight line *d*) have relatively narrower line widths, while regions that lack a cold component have broader line widths. This is another manifestation of the anticorrelation between H I velocity dispersion and H I column density noted by Hunter et al. (2001), which we interpret as due to a pervasive warm component and a spatially varying cold component (Young et al. 2003).

3.3.4. Radio Continuum

As in NGC 2366, most of the radio continuum is related with the supergiant H II region Mrk 59, although it is slightly more extended (Fig. 8a). The 1.4 GHz flux density of Mrk 59 is 10 mJy. Combining this with the 6.3 cm flux of 8.3 ± 0.4 mJy obtained by Klein et al. (1984), we obtain a spectral index of about -0.15. Just as in the case of Mrk 71, the radio continuum emission is predominantly thermal in nature.

3.4. VII Zw 403

The oxygen abundance of the I E BCD VII Zw 403 has been determined by Izotov & Thuan (1999) to be $12 + \log(\text{O}/\text{H}) = 7.69 \pm 0.01$, or $Z_{\odot}/17$. Thuan et al. (1987) have obtained H α Fabry-Pérot interferometric observations of VII Zw 403 and found that the BCD is dominated by eight bright H II regions with diameters between 50–130 pc embedded in fainter diffuse emission. The H α velocity field shows no clear large-scale organized motion but is not completely chaotic either. There is

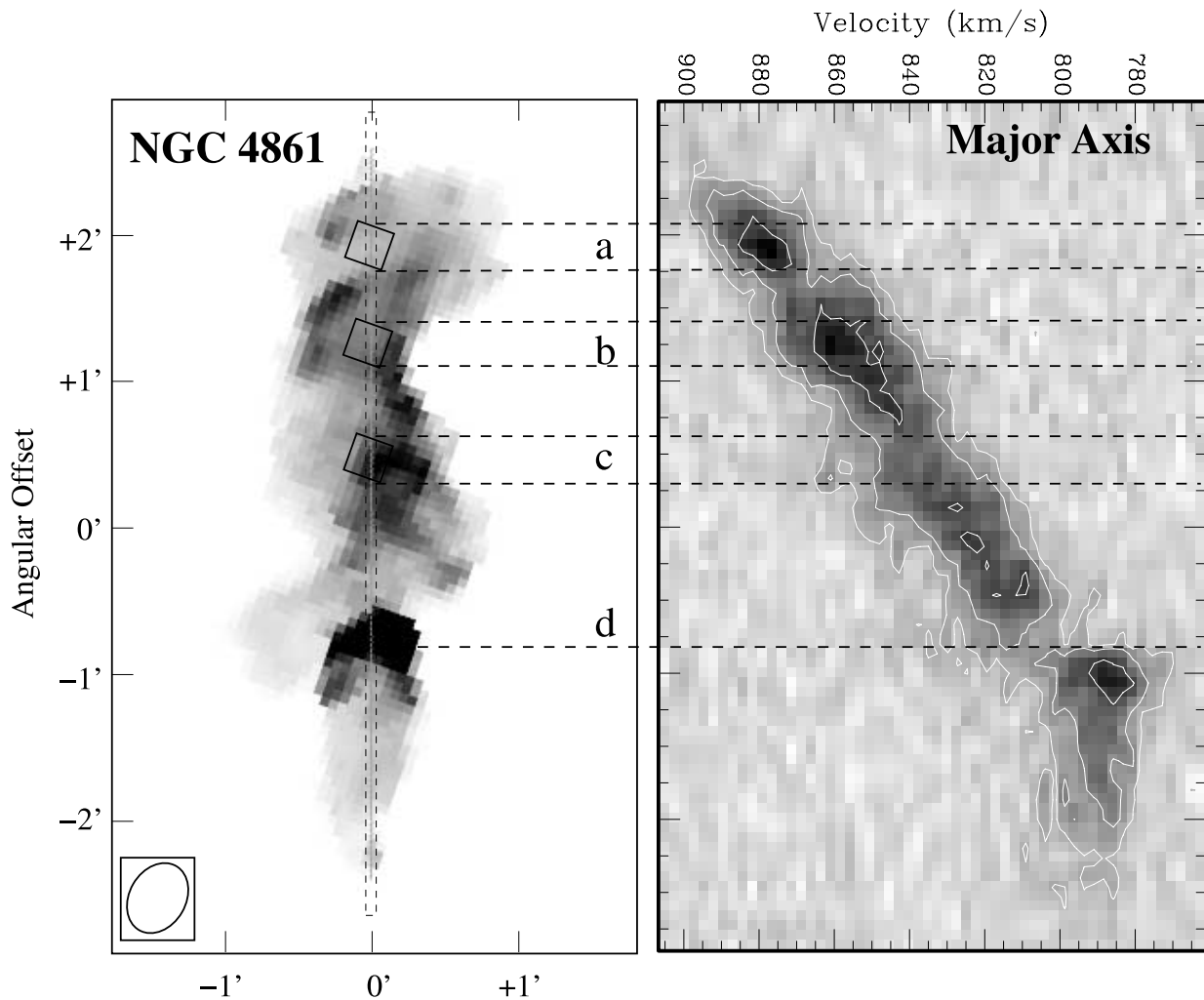


FIG. 13.—NGC 4861 position-velocity map. *Left*: H I second-moment map made from the high-resolution data cube with a vertical rectangular box indicating the location of the position-velocity slice. The second-moment map has been rotated by 19° clockwise to align the slit in the vertical direction. *Right*: Resulting position-velocity slice through the high-resolution data cube. Contours are drawn at $(3, 6, 12) \times 1 \sigma$, where $1 \sigma = 1.2 \text{ mJy beam}^{-1}$. Dashed horizontal lines connect corresponding features in the two maps, and the boxes delineate the regions used to produce the spectra shown in Figs. 14–16.

no overall rotation in the ionized gas, and turbulent random motions must be important. On scales of ~ 450 pc, the $\text{H}\alpha$ velocity field shows evident coherence in directions perpendicular to the major axis. But on smaller scales of ~ 20 pc, there can be velocity jumps of $\sim 30 \text{ km s}^{-1}$. Also, the ionized gas associated with the H II regions, sites of the youngest stellar populations in the BCD tend to have intermediate velocities, while both the highest and lowest velocity areas occur in the diffuse gas between the H II regions. Papaderos et al. (1994) mapped the X-ray emission in VII Zw 403 with the *ROSAT* PSPC, finding the X-rays to be distributed in a central core to which are connected elongated structures extending outside of the optical galaxy. The latter are interpreted as a hot gas outflow from the core of the BCD powered by the present starburst. Schulte-Ladbeck et al. (1998) and Lynds et al. (1998) have used *HST* images to study the stellar content of VII Zw 403. Lynds et al. (1998) found that star formation in the BCD started ~ 1 – 2 Gyr ago, underwent a strong burst ~ 600 – 800 Myr ago, and decreased to the present lower rate. At a distance of 4.5 Mpc, VII Zw 403 is ~ 1.5 Mpc farther away than the main members of the M81 group. At this distance, $1''$ corresponds to 22 pc.

3.4.1. H I Morphology

The VLA results for VII Zw 403 are shown in Figs. 17–20. We recover a flux of about 11 Jy km s^{-1} , or approximately 76% of the TM81 value listed in Table 1 and derived from the H I profile in Figure 6c. The H I intensity map and its comparison to the optical galaxy are shown in the middle row of Figure 17. The H I extent (3.6×2.9 , or $4.7 \text{ kpc} \times 3.8 \text{ kpc}$, at the $5 \times 10^{19} \text{ cm}^{-2}$ contour level) is ~ 4.5 times larger than the optical size of 0.8×0.6 , or $1.0 \text{ kpc} \times 0.8 \text{ kpc}$, at the $B = 25 \text{ mag arcsec}^{-2}$ isophotal level. The optical galaxy is associated with the peak of the H I intensity map, which is slightly off the center defined by the outermost column density contours. The map shows a disturbed H I envelope, which is more extended toward the western edge. We note that the H I intensity map of VII Zw 403 and its relationship with the optical component bears a remarkable resemblance to some of the other iE BCDs studied, for example, by van Zee et al. (1998a), such as UGC 4483, UM 439, UM 461, and UM 462, although the velocity field of VII Zw 403 is considerably more disturbed (see below).

The most interesting feature of the H I envelope of VII Zw 403 is that it appears to have at least two components.

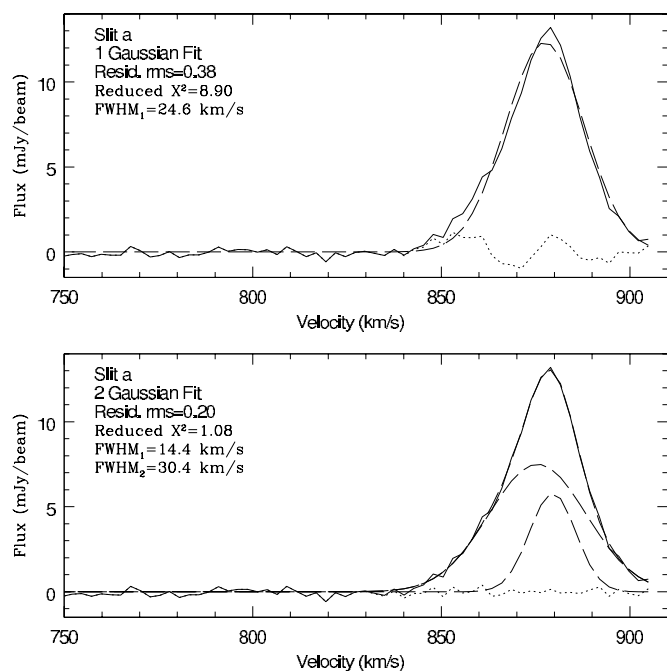


FIG. 14.—Line profile from region *a* in Fig. 13 with results of one-component (*top*) and two-component (*bottom*) Gaussian fits. The solid line represents the observed spectra, the dashed line the Gaussian fit, and the dotted line the residuals of the fit. The rms of the residuals, reduced χ^2 of the fit, and line widths of the Gaussian components are given at the top left corner of each panel.

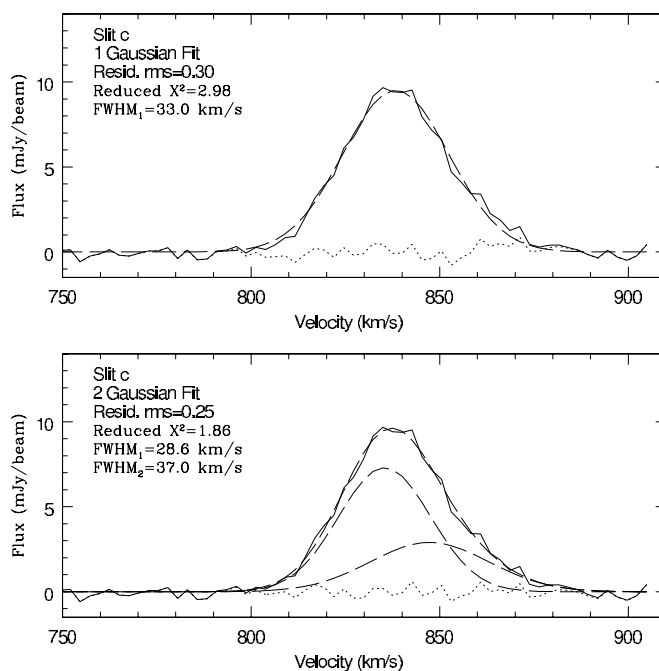


FIG. 16.—Line profile from region *c* in Fig. 13 with results of one-component (*top*) and two-component (*bottom*) Gaussian fits. The solid line represents the observed spectra, the dashed line the Gaussian fit, and the dotted line the residuals of the fit. The rms of the residuals, reduced χ^2 of the fit, and line widths of the Gaussian components are given at the top left corner of each panel.

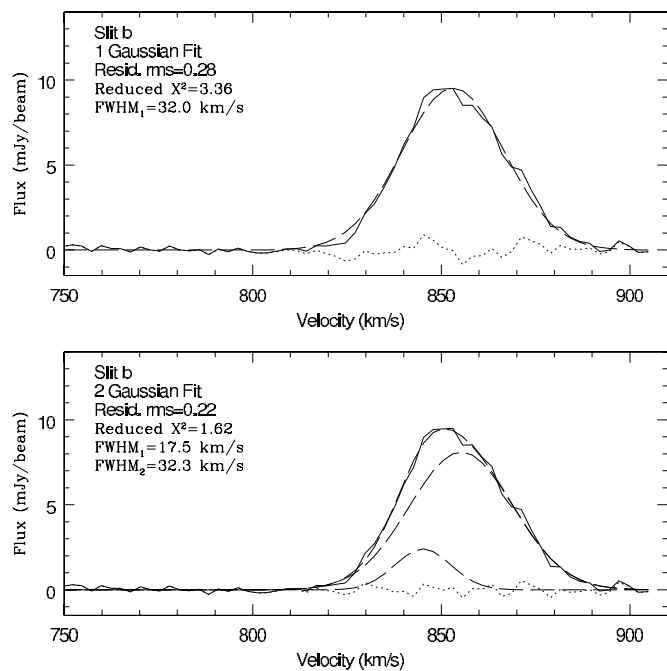


FIG. 15.—Line profile from region *b* in Fig. 13 with results of one-component (*top*) and two-component (*bottom*) Gaussian fits. The solid line represents the observed spectra, the dashed line the Gaussian fit, and the dotted line the residuals of the fit. The rms of the residuals, reduced χ^2 of the fit, and line widths of the Gaussian components are given at the top left corner of each panel.

This is best seen in the high-resolution H I maps (Fig. 18*b*). There seems to be a second density concentration to the north of the brightest H I peak. This gas lies outside the brightest part of the optical body and appears to be associated with the faint ($\mu_B > 24$ mag arcsec⁻²) optical extension to the north (see Fig. 1 of Papaderos et al. 1994). We return to the nature of these components in § 3.4.2.

We have checked whether the H I envelope shows any distinctive feature at the location of the X-ray filaments seen by Papaderos et al. (1994) with *ROSAT*, which they interpreted to be a blowout. Particular attention has been paid to the southeast and southwest X-ray filaments, with respective angular sizes of 2.5' and 4' corresponding to linear sizes of 3.3 and 5 kpc, their detection having been confirmed by a subsequent *ROSAT* HRI frame. While the H I contours do show a slight extension in the southwest direction, the southwest X-ray filament extends beyond the H I envelope. It appears to correspond to a zone of high velocity dispersion oriented in the same direction (Fig. 17*f*).

3.4.2. H I Kinematics

The channel maps for VII Zw 403 (Fig. 19) show evidence of emission over 67 km s⁻¹, and the velocity range in the first-moment map (Fig. 17*e*) is only 29 km s⁻¹. This is much less than for any other of our objects. The velocity contour map (Fig. 17*e*) shows that there is no overall rotation, and we could not fit the velocity field with a Brandt model. Thus, turbulent motions must play a dominant role in the neutral gas, just as they do in the ionized gas in the star-forming region. Figure 17*e* shows velocity jumps of several tens of kilometers per second on scales of 20'', or 440 pc.

Examination of a blowup of the velocity dispersion map (Fig. 18*c*) shows that the high-dispersion region is actually a thin stripe between the two peaks. The velocity dispersion

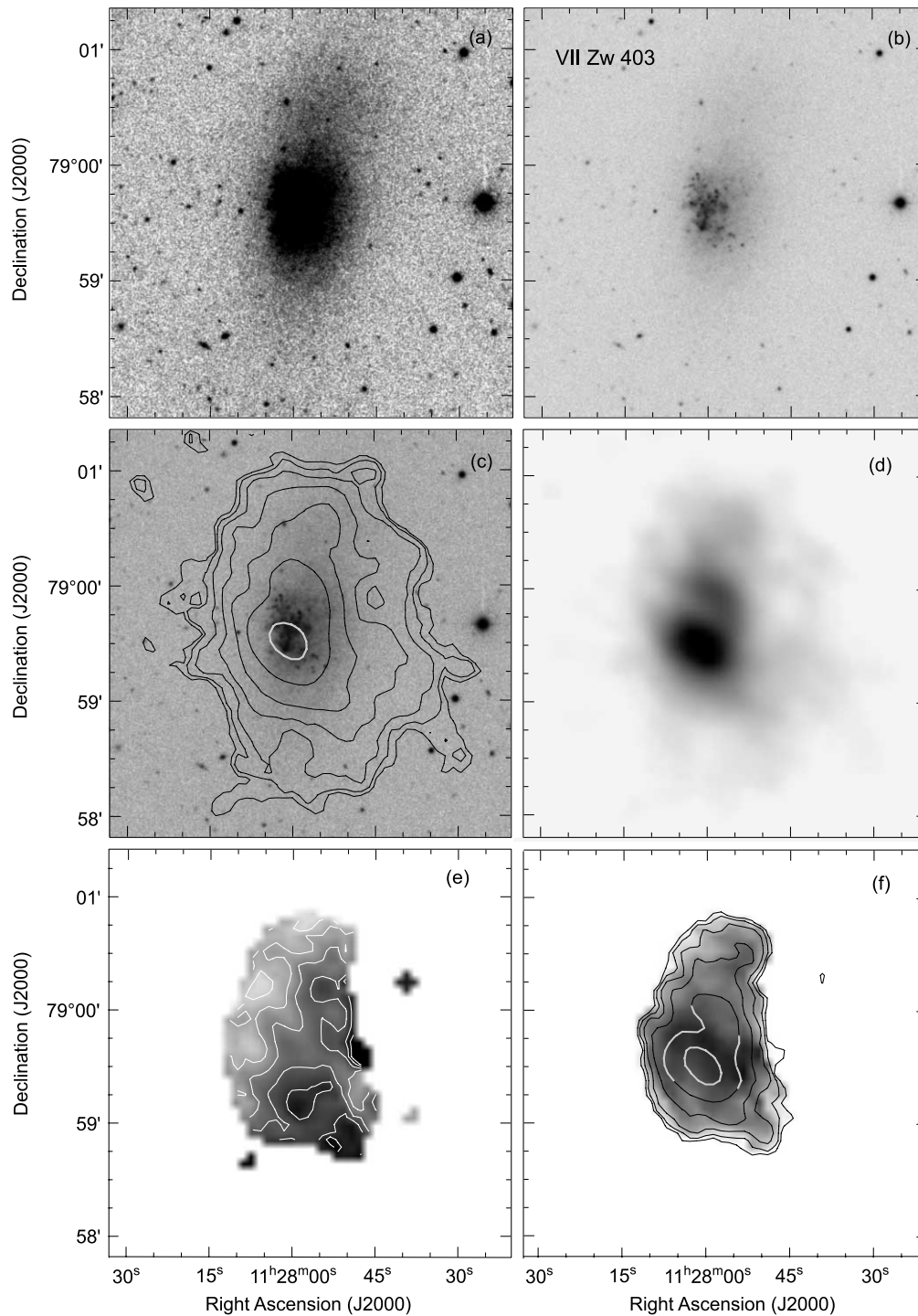


FIG. 17.—VII Zw 403 mosaic. Same layout as in Fig. 1. Contour levels for the low-resolution H I data are $(0.5, 1, 2, 4, 8, 16, 32) \times 10^{20} \text{ cm}^{-2}$, while contours for the high-resolution data are a factor of 2 higher. For the moment 1 map, the isovelocity contours are drawn from -111 km s^{-1} in the northeast to -91 km s^{-1} in the southwest in steps of 4 km s^{-1} .

reaches $\sigma_{\text{peak}} = 12.7 \text{ km s}^{-1}$ in this region, while the mean is $\sigma = 7.8 \text{ km s}^{-1}$.

More details arise when looking at various position-velocity plots. In Figure 20 we show such plots taken along three different position angles: through both components (slice a) and roughly perpendicular to them along directions of maximum velocity gradient (slices b and c). In each position-velocity plot in Figure 20, we label where the velocity slice crosses one of the other slices by the appropriate letter. The position-velocity plot through the two components (major axis slice a) shows

that they share kinematics: both the mean velocity and the spread of velocities is similar. It also illustrates that the high velocity dispersion seen between the two components in Figure 18c is due to the lack of dense gas, rather than to an increased velocity spread of the H I, just as we found in NGC 4861 and NGC 2366.

Interestingly, the profiles along positions b and c in Figure 20 show a coherent velocity gradient, as if the gas is rotating like a cylinder around the major axis with a maximum velocity V_{max} of about 20 km s^{-1} . This would give an upper limit to

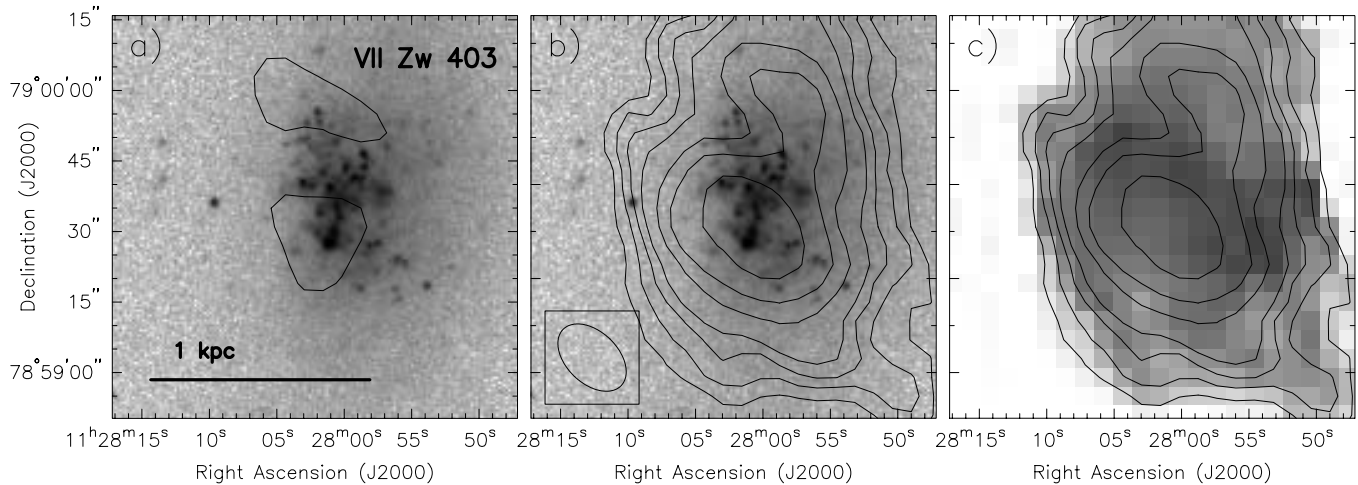


FIG. 18.—Detailed comparison between the radio and optical properties of the major star-forming regions in VII Zw 403. (a) 1.4 GHz radio continuum emission contours superposed on a gray-scale depiction of the optical CCD image. Contours are drawn at $(-2.5, 2.5) \times 1 \sigma$ ($0.22 \text{ mJy beam}^{-1}$). (b) Contours of the integrated H I emission from the high-resolution data superposed on the optical image. Contours are drawn at $(-2.5, 2.5, 5, 7.5, 10, 15, 20, 30) \times 10^{20} \text{ cm}^{-2}$. The boxed ellipse indicates the FWHM beam size for the H I data. (c) The same H I column density contours superposed on a gray-scale representation of the high-resolution H I velocity dispersion map in which the darkest shade corresponds to a dispersion of 13 km s^{-1} .

V_{tot}/σ of about 2.5 (Table 3). The morphology of the H I makes it difficult to understand this gradient in terms of circular disk motion.

3.4.3. Radio Continuum

The 1.4 GHz continuum flux is rather weak, with a peak of only $0.9 \text{ mJy beam}^{-1}$ and a total flux of 2.5 mJy. The strongest peak is associated with the star-forming region in VII Zw 403, and there is a hint of an extension to the north (Fig. 18, left). However, the extended emission is of low significance ($\sim 3 \sigma$). We cannot derive a spectral index as there exists no radio continuum measurement at another frequency.

3.5. Haro 2

Haro 2 (\equiv Mrk 33 \equiv Arp 233) has the shape and brightness profile of a low-luminosity elliptical galaxy with a very bright and blue nucleus exhibiting intense star formation (Loose & Thuan 1986). Compared with the three previous BCDs, Haro 2 is relatively more metal-rich. Davidge (1989) determined its metallicity to be $\frac{1}{3}$ to $\frac{1}{2}$ that of the Sun. Fanelli et al. (1988) have performed spectral synthesis of the UV spectrum of the nucleus and shown that the present burst has been preceded by at least two other bursts separated by several Gyr. The UV spectrum shows Si IV and C IV P Cygni profiles, indicating the presence of hot massive stars with stellar winds. Mas-Hesse & Kunth (1999) estimate an age of $\sim 6 \text{ Myr}$ for the latest burst, consistent with the presence of Wolf-Rayet stars. Lequeux et al. (1995) have found in a UV *HST* spectrum N I, Si II, and Si III lines blueshifted by $\sim 200 \text{ km s}^{-1}$ with respect to the H I gas. They interpret these absorption lines as originating in a galactic wind flowing away from the star-forming region at a velocity of 200 km s^{-1} . The column density of neutral hydrogen in the outflowing gas is $7 \times 10^{19} \text{ cm}^{-2}$, only a minute fraction of the total column density of $\sim 2 \times 10^{21} \text{ cm}^{-2}$. The total expanding mass is $\sim 10^7 M_{\odot}$ if distributed in a spherical shell. Its metallicity is between $\frac{1}{30}$ and $\frac{1}{3}$ that of the Sun, with the higher range of values more likely. Haro 2 has been detected in CO (Sage et al. 1992; Israel et al. 1995) and in the far-infrared by *IRAS* (Kunth & Sèvre 1985). CO mapping by Fritz et al. (2001) shows a relatively strong central peak and two lobes extending

along the major axis of the star-forming region. The emission of the molecular gas exhibits a very disturbed velocity field with steep gradients, suggesting perhaps a recent merger. A VLA C+D configuration H I map and a CO map of Haro 2 have also been obtained by Bravo-Alfaro et al. (2004). At a distance of 24.5 Mpc, $1''$ corresponds to a linear size of 119 pc.

3.5.1. H I Morphology

Haro 2 being the most distant galaxy in the present sample, its H I map has the poorest resolution, and there is comparatively less detail. Our measured flux (3.4 Jy km s^{-1}) represents 77% of the single-dish flux obtained by TM81 (see Fig. 6d). The total intensity map and its comparison with the optical galaxy are shown in Figures 21c–21d. The deconvolved H I size is $\sim 1.8 \times 0.9$ at the $5 \times 10^{19} \text{ cm}^{-2}$ contour level, or $13.1 \text{ kpc} \times 6.5 \text{ kpc}$. This is to be compared to the optical size of $64'' \times 44''$, or $7.6 \text{ kpc} \times 5.2 \text{ kpc}$, at the $B = 25 \text{ mag arcsec}^{-2}$ isophotal level (Loose & Thuan 1986). Thus, the H I envelope is less extended relative to the optical galaxy than in the other three systems.

At low resolution, the H I distribution is elongated in the southeast-northwest direction, the same direction as the optical component. While the latter has a regular elliptical shape (Loose & Thuan 1986), the H I component shows irregularities, especially at the southeastern end, which is linear rather than elliptical in shape. Because of this asymmetry, the optical center is south of the H I center. The high-resolution map in Figure 22b shows that there are actually two components to the H I distribution: an irregular distribution centered on the star-forming region and a clump at $\sim 28''$ to the northwest. The northwestern component is still within the optical elliptical component as shown by the deep optical stretch of Figure 21a but is not associated with any discrete optical feature. The light is redder there, indicating older stellar populations (Loose & Thuan 1986).

There is also a companion H I cloud to the northeast. This feature is quite faint but is detected at the 3σ level in at least four adjacent channels ($V = 1460\text{--}1492 \text{ km s}^{-1}$ in Fig. 23). This cloud is also seen in the VLA C+D configuration map presented by Bravo-Alfaro et al. (2004), although the

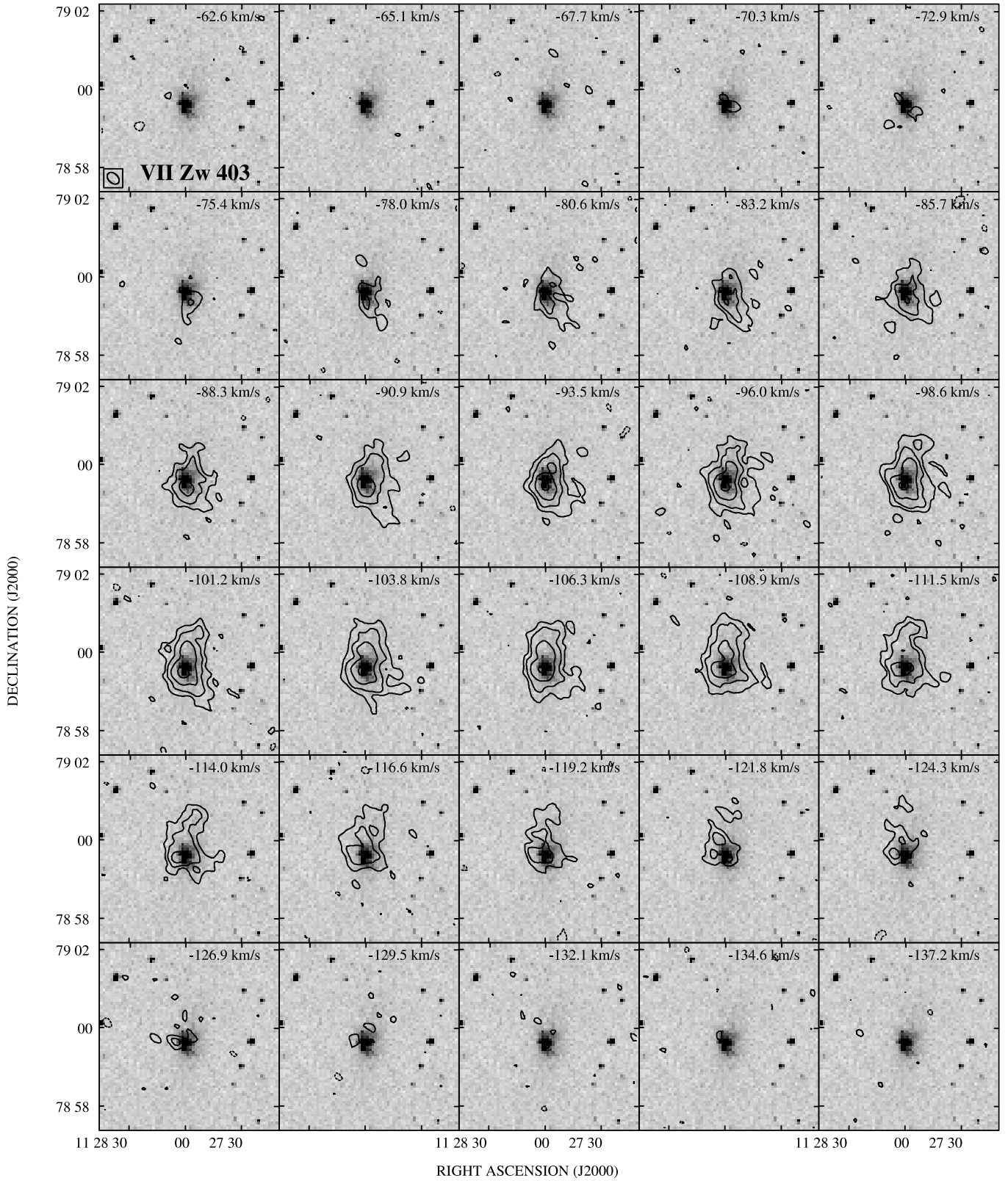


FIG. 19.—Low-resolution H I channel map contours of VII Zw 403 superposed on a gray-scale representation of the DSS optical image. The resolution is indicated in the lower left corner of the first panel (*top left*). The channel spacing is 2.5 km s^{-1} , with the heliocentric velocity of the channel printed in the top right corner of each panel. Contours are drawn at $(-3, 3, 6, 12, 24) \times 1 \sigma$, where $1 \sigma = 1.3 \text{ mJy beam}^{-1} = 1.2 \times 10^{20} \text{ cm}^{-2}$.

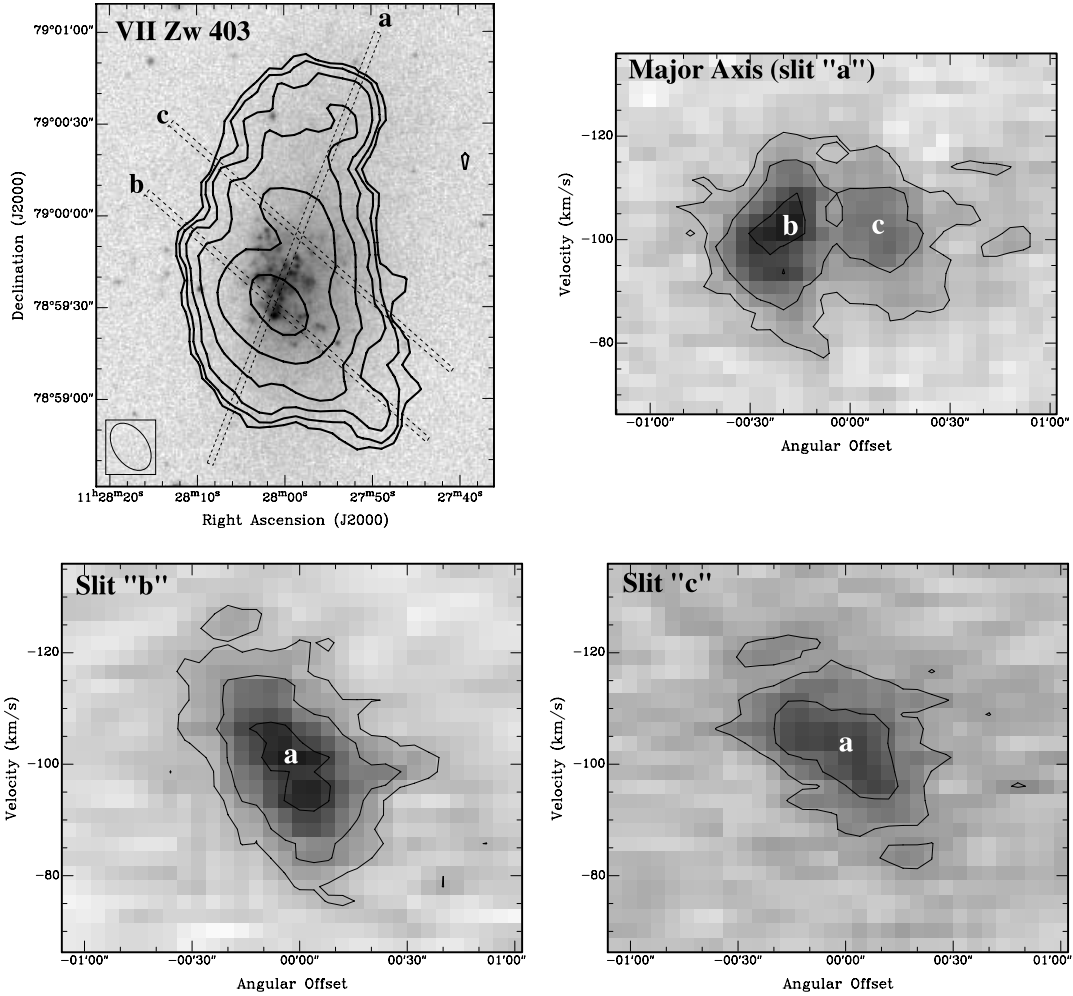


FIG. 20.—VII Zw 403 position-velocity maps. *Top left*: Optical CCD image with contours from the high-resolution data cube superposed. Contours are drawn at $(1, 2, 4, 8, 16, 32) \times 17.1 \text{ mJy beam}^{-1} \text{ km s}^{-1}$, where the lowest contour corresponds to a column density of $1 \times 10^{20} \text{ cm}^{-2}$. The three narrow elongated rectangular boxes represent the location of the three slits a, b, and c where position-velocity profiles were derived. *Top right*: Position-velocity profile for slit location a. The white letters b and c indicate where slits b and c intersect with slit a. *Bottom left*: Position-velocity profile for slit location b. The white letter a indicates where slit a intersects with slit b. *Bottom right*: Position-velocity profile for slit location c. The white letter a indicates where slit a intersects with slit c. In the position-velocity plots, contours are drawn at $(3, 6, 12) \times 1 \sigma$, where $1 \sigma = 1.8 \text{ mJy beam}^{-1}$.

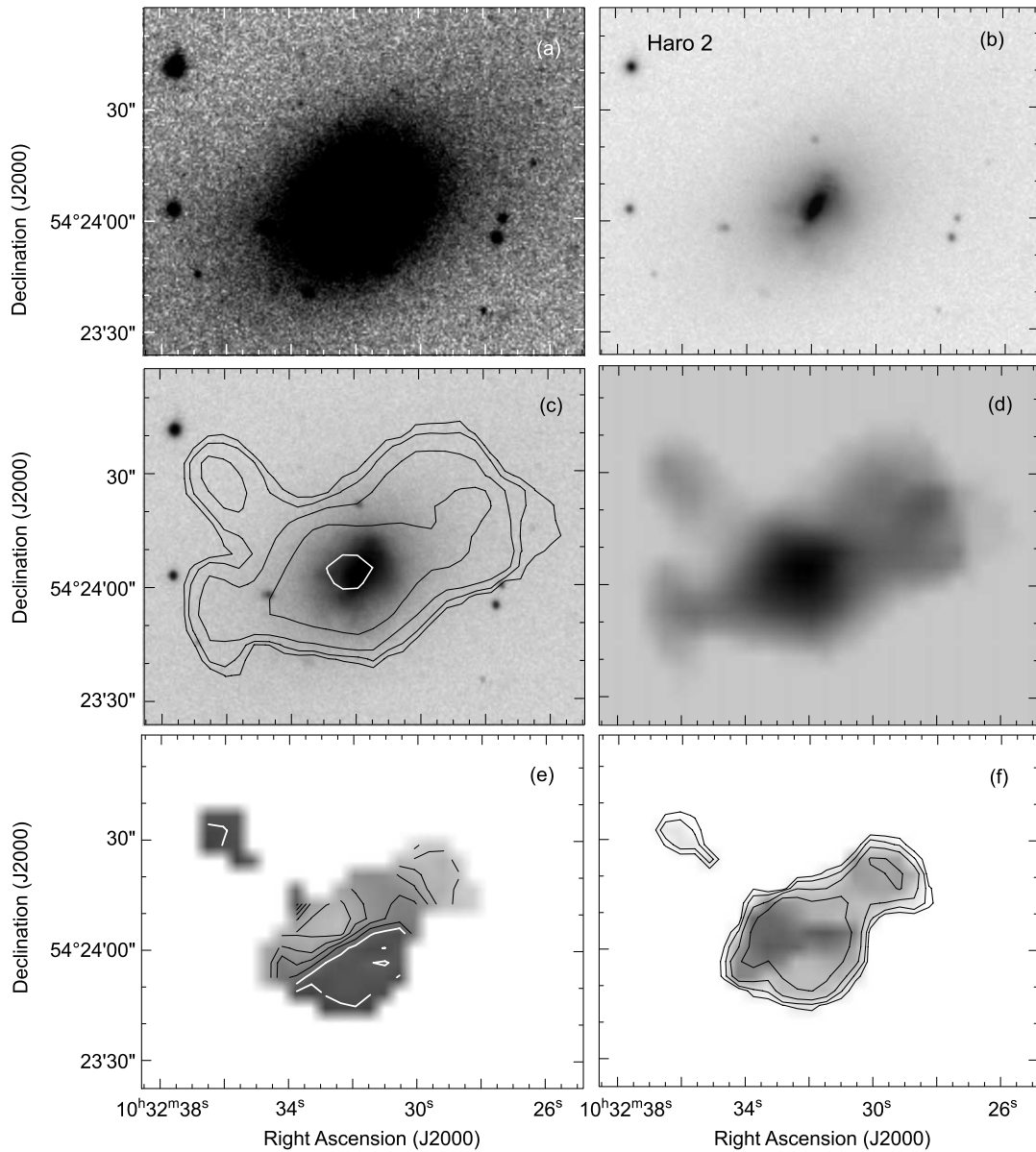


FIG. 21.—Haro 2 mosaic. Same layout as in Fig. 1. Contour levels for both the high- and low-resolution H I data are $(0.5, 1, 2, 4, 8, 16, 32) \times 10^{20} \text{ cm}^{-2}$. For the moment 1 map, the isovelocity contours are drawn from 1405 km s^{-1} in the north to 1475 km s^{-1} in the south in steps of 10 km s^{-1} .

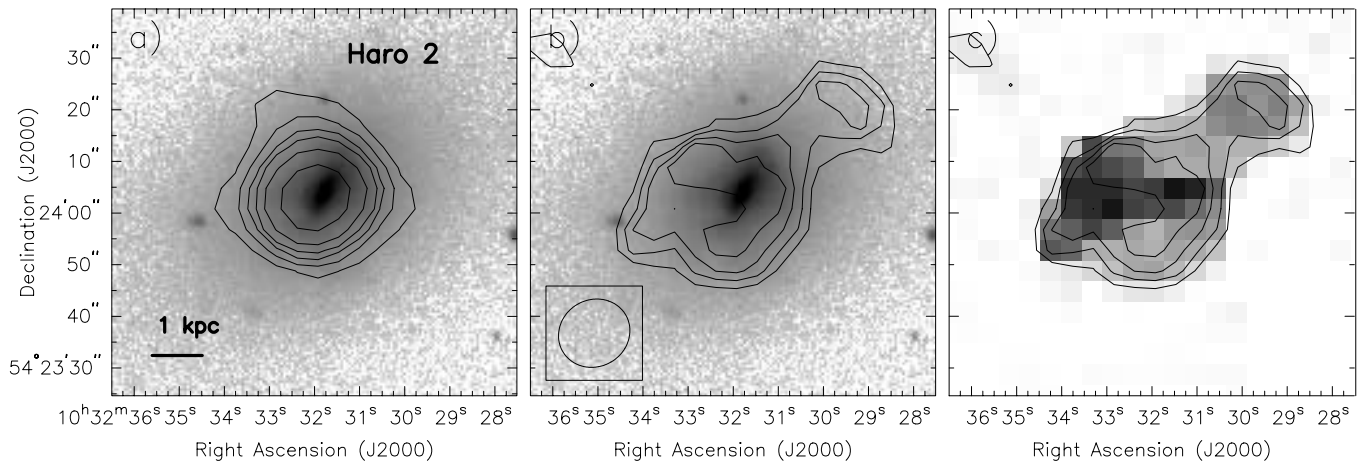


FIG. 22.—Detailed comparison between the radio and optical properties of the major star-forming regions in Haro 2. (a) 1.4 GHz radio continuum emission contours superposed on a gray-scale depiction of the optical CCD image. Contours are drawn at $(-2.5, 2.5, 5, 7.5, 10, 15, 20) \times 1 \sigma$ ($0.33 \text{ mJy beam}^{-1}$). (b) Contours of the integrated H I emission from the high-resolution data superposed on the optical image. Contours are drawn at $(-2.5, 2.5, 5, 7.5, 10) \times 10^{20} \text{ cm}^{-2}$. The boxed ellipse indicates the FWHM beam size for the H I data. (c) The same H I column density contours superposed on a gray-scale representation of the high-resolution H I dispersion map in which the darkest shade corresponds to a dispersion of 32 km s^{-1} .

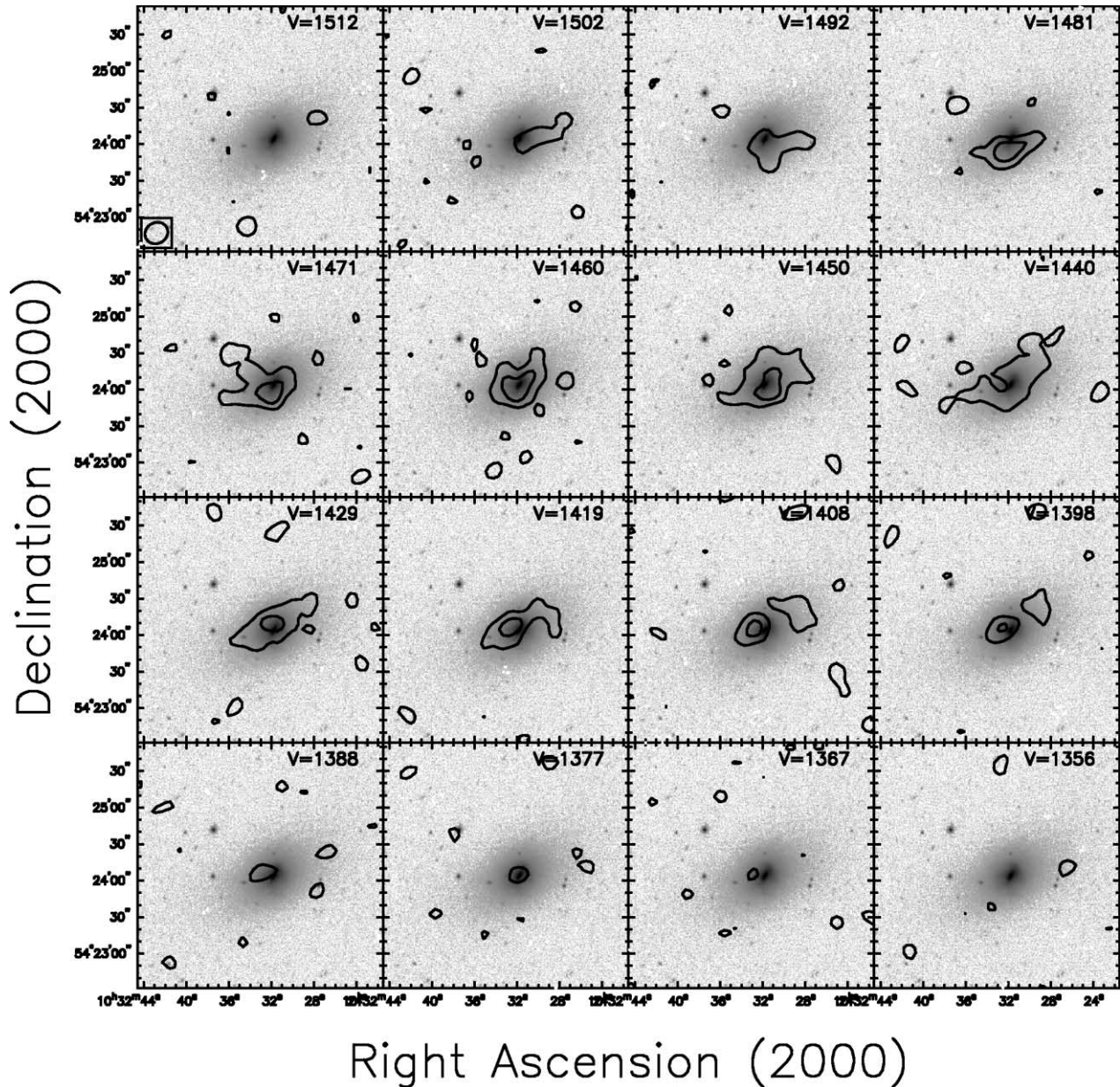


FIG. 23.—Low-resolution H I channel map contours of Haro 2 superposed on a gray-scale representation of the CCD optical image. The resolution is indicated in the lower left corner of the first panel (*top left*). The channel spacing is 10.4 km s^{-1} , with the heliocentric velocity of the channel printed in the upper right corner of each panel. Contours are drawn at $(-3, 3, 6) \times 1 \sigma$, where $1 \sigma = 0.84 \text{ mJy beam}^{-1} = 2.9 \times 10^{20} \text{ cm}^{-2}$.

morphology is somewhat different: in the Bravo-Alfaro et al. map, the cloud does not extend as far to the northeast as our contours indicate. Bravo-Alfaro et al. detect other H I features that are fainter than our sensitivity limit. These include several other H I clouds, or extensions, originating from the H I envelope around Haro 2, as well as H I gas associated with an optically faint spheroidal system just to the northeast of the H I cloud we detect (seen in upper left corner of Fig. 21c).

The H I mass of the H I cloud is $2 \times 10^7 M_{\odot}$, compared with $3.4 \times 10^8 M_{\odot}$ for the main body. The cloud has no optical counterpart on our CCD *B* image or on the DSS and appears similar to the H I companions seen near other BCDs (cf. NGC 4861 above, Taylor et al. 1994). The observations of Bravo-Alfaro et al. suggest that it might be tidally related to the optical companion to the northeast.

3.5.2. H I Kinematics

No kinematical modeling was possible for Haro 2 as the spatial resolution is too poor to obtain a reasonable number of points for a rotation curve, making the algorithm we used highly unstable.

As mentioned above, the H I northeast cloud appears in the channel maps at velocities between $1460\text{--}1492 \text{ km s}^{-1}$ (Fig. 23). There is a H I bridge connecting it to Haro 2, which is visible in the channel map at 1471 km s^{-1} and also in the total intensity maps (Figs. 21c and 21d). The companion to the northeast has been tentatively detected in H I by Bravo-Alfaro et al. (2004) at velocities of $1422\text{--}1443 \text{ km s}^{-1}$. As for the northwest structure, it is seen over a broader range of velocities, from 1400 to 1440 km s^{-1} .

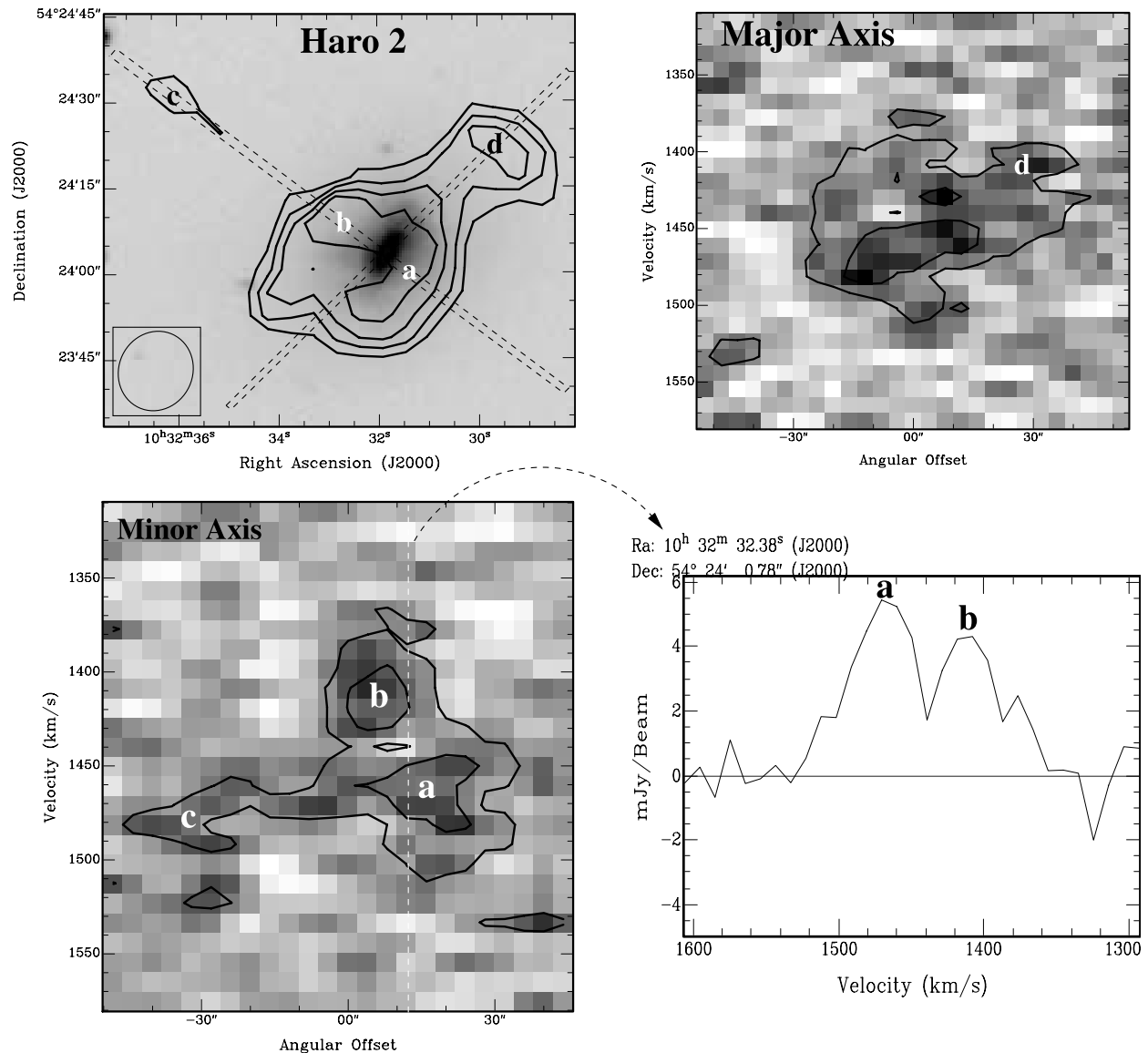


FIG. 24.—Haro 2 position-velocity plots. *Top left*: High-resolution H I data contours superposed on the optical CCD image. Contours are drawn at $(-2.5, 2.5, 5, 7.5, 10) \times 10^{20} \text{ cm}^{-2}$. The slits for which position-velocity profiles have been derived are aligned along the optical major and minor axes. They are indicated by elongated dashed rectangles. The location of various components are labeled “a”, “b”, “c”, and “d”. *Top right*: Position-velocity profile along the major axis. The location of component “d” is labeled. *Bottom left*: Position-velocity profile along the minor axis. The positions of components “a”, “b”, and “c” are labeled. The location of the spectrum shown in the bottom right panel is indicated by a dashed white line and arrow. *Bottom right*: Spectrum of the central location [R.A.(J2000.0) = $10^{\text{h}}32^{\text{m}}32^{\text{s}}.38$, decl.(J2000.0) = $54^{\circ}24'07.78''$] showing a double-peaked line profile.

The mean velocity dispersion is significantly high, $\sigma = 16.1 \text{ km s}^{-1}$ with peaks as high as $\sim 30 \text{ km s}^{-1}$. However, with the low spatial resolution we have for Haro 2, this may be the result of beam smearing, because different unresolved parts of the galaxy with different velocities might combine together to produce a broad line. Additionally, the profiles are complicated and often double-peaked, as seen in the position-velocity plots presented in Figure 24. In this figure, position-velocity profiles are extracted along the optical major and minor axis. Several locations along both slits are labeled from “a” to “d”.

Along the major axis slit, there is a slight rotational gradient in the higher density contours, but overall the gas shows very little ordered motion. The higher density region with the linear velocity gradient is likely associated with the CO disk imaged by Fritz et al. (2001) and Bravo-Alfaro et al. (2004), which is aligned along this direction and shows indications of rotation.

Along the minor axis slit there are two separate kinematic components that correspond to opposite sides of the H I ringlike structure seen in the high-resolution moment map (Fig. 22b and labeled “a” and “b” in Fig. 24). This would seem to indicate that the H I rotates around the major axis of the galaxy, with a maximum velocity of $\sim 65 \text{ km s}^{-1}$. If this interpretation is correct, this would correspond to a maximum V_{rot}/σ of 4.0 (Table 3). However, the H I line profiles are complicated and often double valued, as shown in a spectra taken through the center of Haro 2 and plotted in the lower right panel of Figure 24. Instead of ordered minor axis rotation, it is possible that we are seeing multiple gaseous features either falling in or being blown out. Higher resolution H I observations are required to make more sense of the gas kinematics in this system. Finally, along the minor axis slit we also see the emission associated with the H I cloud (labeled “c” in Fig. 24).

3.5.3. Radio Continuum

The continuum map is shown in Figure 22a. Again all the 21 cm continuum flux of Haro 2, which is 19 mJy, is associated with the star-forming region. Combining with the 6.3 cm flux density of 12 ± 1 mJy obtained by Klein et al. (1984) gives a spectral index of -0.38 , similar to the average value of -0.33 obtained by Klein et al. for a large sample of BCDs. While thermal radio emission is still dominant in Haro 2, the steeper index as compared to NGC 2366 and NGC 4861 implies a slightly larger fraction of nonthermal emission due to supernova remnants, suggesting that the starburst in Haro 2 is slightly older than those in Mrk 71 and Mrk 59. Again, there is a slight displacement ($\sim 2''$) of the radio continuum source to the southeast of the optical center.

4. CONCLUSIONS

Summarizing the preceding detailed presentation of each of these four systems, we note the following general trends:

1. The active regions of star formation as characterized by bright H II regions are associated with regions of high H I column densities. However, there are displacements of $\lesssim 0.8$ kpc between the neutral gas and stellar peaks in NGC 2366 and NGC 4861, similar to those discussed by Viallefond & Thuan (1983), van Zee et al. (1998a), and Pustilnik et al. (2001) in other H I maps of BCDs. These displacements are probably the result of mechanical energy injected into the ISM by SNe evacuating the neutral gas or of UV photons from hot massive stars (both galaxies contain Wolf-Rayet stars) ionizing it. Other signs of the disruptive influence of massive star formation on the ISM of BCDs are the presence of H I clumps in NGC 2366 and NGC 4861, of H I minima in NGC 2366, and the occurrence of zones of high velocity dispersion gas near regions of active star formation.

2. The cometary-like galaxies NGC 2366 ($M_B = -16.7$) and NGC 4861 ($M_B = -18.0$) have regular kinematics, either rotational or barlike, although we favor the former hypothesis as there is no photometric signature of a bar in either galaxy. Their rotational kinematics (a linear rise followed by a flattening of the rotation curve) are similar to that found by van Zee et al. (1998a) for fainter BCDs ($-16 \lesssim M_B \lesssim -13$). Both galaxies are rotationally dominated, as the ratios of maximum rotational velocity to velocity dispersion are, respectively, 8.7 and 6.4 in NGC 2366 and NGC 4861. On the other hand, the velocity fields of the other two systems, the iE BCD VII Zw 403 ($M_B = -14.2$) and the nE BCD Haro 2 ($M_B = -18.6$), lack rotational regularity. There is suggestion that there may be rotation not around the minor axis, as is usually the case, but around the major axis. The ratios of maximum rotational velocity to velocity dispersion are considerably lower, less than 2.5 and 4.0 for VII Zw 403 and Haro 2, respectively. Thus the BCD phenomenon does not require necessarily a regular rotational field. Alternatively, there may have been a regular rotation that has been destroyed by the energy input of the starburst.

3. The H I distribution is centrally peaked in VII Zw 403 and Haro 2, as in other iE-type BCDs discussed by Taylor et al. (1994) and van Zee et al. (1998a). This appears to be a general property of iE and nE-type BCDs, the most common ones. By

contrast, cometary-type BCDs possess multiple H I peaks that are not centrally located but are scattered over the disk. In that sense, they resemble more the low surface brightness dwarf irregular galaxies studied by Simpson & Gottesman (2000) and Young et al. (2003).

4. In NGC 2366 and NGC 4861, we found a tendency for H I gas with higher velocity dispersion to be associated with regions of lower H I column density. Hunter et al. (2001) attributed this anticorrelation to long-range turbulence. Our data support rather the point of view of Young et al. (2003) in which the anticorrelation between H I velocity dispersion and column density is naturally explained in the context of the standard two-phase model of the ISM (see also Braun 1995, 1997). In this model, the cold neutral medium resides in the central regions of the galaxy and possesses a smaller scale height and velocity dispersion, and a higher column density. This component is in pressure equilibrium with the more diffuse and extended warm neutral medium, which has a larger scale height and velocity dispersion, and a lower column density.

5. In all BCDs, the radio continuum emission is predominantly thermal and is associated with the starburst regions.

6. H I clouds with no discernible optical counterpart have been found in the surroundings of NGC 4861 and Haro 2. The nature of such H I clouds is not clear. Taylor et al. (1994) suggest that they may be responsible for the present episodes of star formation in their dwarf hosts. In NGC 4861, there is an extended envelope of H I directed toward the cloud. If these features are purely gaseous, then given the mass of the cloud and that of the envelope ($M_e/M_c \simeq 10$, §3.3.1), it seems highly unlikely that the cloud could have pulled the envelope out of the galaxy. Nevertheless, the fact that the envelope is oriented toward the cloud suggests that these two features may have a common origin. They may be remnants of a previous interaction with a larger object or may have been expelled by a starburst event. The cloud in Haro 2 extends toward a small optical companion, which has recently been tentatively detected in H I by Bravo-Alfaro et al. (2004), suggesting a possible tidal origin.

We thank Patricia Smiley of NRAO for help with the figures. T. X. T. acknowledges the financial support of NSF grant AST 02-05785. We are grateful to Polis Papaderos for providing the CCD images. We thank the referee for the time and effort put into reviewing this paper. Some figures were made with the WIP interactive software package (Morgan 1995). This research has made extensive use of the NASA/IPAC Extragalactic Database (NED), which is operated by the Jet Propulsion Laboratory, California Institute of Technology, under contract with the National Aeronautics and Space Administration. The Digitized Sky Surveys were produced at the Space Telescope Science Institute under US Government grant NAG W-2166. The images of these surveys are based on photographic data obtained using the Oschin Schmidt Telescope on Palomar Mountain and the UK Schmidt Telescope. The plates were processed into the present compressed digital form with the permission of these institutions.

REFERENCES

- Arp, H. C. 1966, *ApJS*, 14, 1
 Barth, C. S., Cepa, J., Vilchez, J. M., & Dottori, H. A. 1994, *AJ*, 108, 2069
 Bosma, A. 1981, *AJ*, 86, 1825
 Brandt, J. C. 1960, *ApJ*, 131, 293
 Braun, R. 1995, *A&AS*, 114, 409
 ———. 1997, *ApJ*, 484, 637
 Bravo-Alfaro, H., Brinks, E., Baker, A. J., Walter, F., & Kunth, D. 2004, *AJ*, 127, 264

- Briggs, D. S. 1995, Ph.D. thesis, New Mexico Inst. Mining Technology
- Calzetti, D. 1997, *AJ*, 113, 162
- Clark, B. G. 1980, *A&A*, 89, 377
- Cornwell, T. J., Uson, J. M., & Haddad, N. 1992, *A&A*, 258, 583
- Davidge, T. 1989, *PASP*, 101, 494
- de Vaucouleurs, G., de Vaucouleurs, A., Corwin, H. G., Jr., Buta, R. J., Paturel, G., & Fouqué, P. 1991, *Third Reference Catalog of Bright Galaxies* (New York: Springer)
- Dickel, J. R., & Rood, H. J. 1978, *ApJ*, 223, 391
- Dinerstein, H. L., & Shields, G. A. 1986, *ApJ*, 311, 45
- Drissen, L., Roy, J.-R., Robert, C., Devost, D., & Doyon, R. 2000, *AJ*, 119, 688
- Fanelli, M. N., O'Connell, R. W., & Thuan, T. X. 1988, *ApJ*, 334, 665
- Fomalont, E. B., & Perley, R. A. 1999, in *ASP Conf. Ser. 180, Synthesis Imaging in Radio Astronomy*, ed. G. B. Taylor, C. L. Carilli, & R. A. Perley (San Francisco: ASP), 79
- Fraternali, F., van Moorsel, G., Sancisi, R., & Oosterloo, T. 2002, *AJ*, 123, 3124
- Fritz, T., Huttemeister, S., Neiningner, N., & Klein, U. 2001, in *The Magellanic Clouds and Other Dwarf Galaxies*, ed. K. S. De Boer, R.-J. Dettmar, & U. Klein (Aachen: Shaker), 137
- Guseva, N. G., Izotov, Y. I., & Thuan, T. X. 2000, *ApJ*, 531, 776
- Heckman, T. M., Robert, C., Leitherer, C., Garnett, D. R., & van der Rydt, F. 1998, *ApJ*, 503, 646
- Heiles, C., & Troland, T. H. 2003, *ApJS*, 145, 329
- Huchtmeier, W. K., Seiradakis, J. H., & Materne, J. H. 1981, *A&A*, 102, 134
- Hunter, D. A., Elmegreen, B. G., & van Woerden, H. 2001, *ApJ*, 556, 773
- Hunter, D. A., Wilcots, E. M., van Woerden, H., Gallagher, J. S., & Kohle, S. 1998, *ApJ*, 495, L47
- Israel, F. P., Tacconi, L. J., & Baas, F. 1995, *A&A*, 295, 599
- Izotov, Y. I., & Thuan, T. X. 1999, *ApJ*, 511, 639
- Izotov, Y. I., Thuan, T. X., & Lipovetsky, V. A. 1997, *ApJS*, 108, 1
- Kennicutt, R. C., Balick, B., & Heckman, T. 1980, *PASP*, 92, 134
- Klein, U., Wielebinski, R., & Thuan, T. X. 1984, *A&A*, 141, 241
- Kunth, D., & Sève, F. 1985, in *Star-forming Dwarf Galaxies and Related Objects*, ed. D. Kunth, T. X. Thuan, & J. T. T. Van (Gif-sur-Yvette: Ed. Frontières), 331
- Lee, J. C., Salzer, J. J., Impey, C., Thuan, T. X., & Gronwall, C. 2002, *AJ*, 124, 3088
- Lequeux, J., Kunth, D., Mas-Hesse, J. M., & Sargent, W. L. W. 1995, *A&A*, 301, 18
- Lequeux, J., & Viallefond, F. 1980, *A&A*, 91, 269
- Lo, K. Y., Sargent, W. L. W., & Young, K. 1993, *AJ*, 106, 507
- Loose, H.-H., & Thuan, T. X. 1985, in *Star-forming Dwarf Galaxies and Related Objects*, ed. D. Kunth, T. X. Thuan, & J. T. T. Van (Gif-sur-Yvette: Ed. Frontières), 73
- . 1986, *ApJ*, 309, 59
- Lynds, R., Tolstoy, E., O'Neil, E., & Hunter, D. A. 1998, *AJ*, 116, 146
- Mas-Hesse, J. M., & Kunth, D. 1999, *A&A*, 349, 765
- McKee, C. F., & Ostriker, J. P. 1977, *ApJ*, 218, 148
- Morgan, J. A. 1995, in *ASP Conf. Ser. 77, Astronomical Data Analysis Software and Systems IV*, ed. R. A. Show, H. E. Payne, & J. J. E. Hayes (San Francisco: ASP), 129
- Napier, P. J., Thompson, A. R., & Ekers, R. D. 1983, *Proc. IEEE*, 71, 1295
- Noeske, K. G., Guseva, N. G., Fricke, K. J., Izotov, Y. I., Papaderos, P., & Thuan, T. X. 2000, *A&A*, 361, 33
- Papaderos, P., Fricke, K. J., Thuan, T. X., & Loose, H.-H. 1994, *A&A*, 291, L13
- Pustilnik, S. A., Brinks, E., Thuan, T. X., Lipovetsky, V. A., & Izotov, Y. I. 2001, *AJ*, 121, 1413
- Roy, J.-R., Belley, J., Dutil, Y., & Martin, P. 1996, *ApJ*, 460, 284
- Roy, J.-R., Boulesteix, J., & Grundseth, B. 1991, *ApJ*, 367, 141
- Rupen, M. P. 1999, in *ASP Conf. Ser. 180, Synthesis Imaging in Radio Astronomy*, ed. G. B. Taylor, C. L. Carilli, & R. A. Perley (San Francisco: ASP), 229
- Sage, L. J., Salzer, J. J., Loose, H.-H., & Henkel, C. 1992, *A&A*, 265, 19
- Salzer, J. J., Rosenberg, J. L., Weisstein, E. W., Mazzarella, J. M., & Bothun, G. D. 2002, *AJ*, 124, 191
- Schechter, P. 1980, *AJ*, 85, 801
- Schlegel, D. J., Finkbeiner, D. P., & Davis, M. 1998, *ApJ*, 500, 525
- Schulte-Ladbeck, R. E., Crone, M. M., & Hopp, U. 1998, *ApJ*, 493, L23
- Simpson, C. E., & Gottesman, S. T. 2000, *AJ*, 120, 2975
- Skillman, E. D., Terlevich, R., Teuben, P. J., & van Woerden, H. 1988, *A&A*, 198, 33
- Swaters, R. A. 1999, Ph.D. thesis, Univ. Groningen
- Swaters, R. A., Sancisi, R., & van der Hulst, J. M. 1997, *ApJ*, 491, 140
- Taylor, C. L., Brinks, E., Pogge, R. W., & Skillman, E. D. 1994, *AJ*, 107, 971
- Thuan, T. X., Balkowski, C., Cayatte, V., & Van, J. T. T. 1998, eds. *Dwarf Galaxies and Cosmology* (Gif-sur-Yvette: Ed. Frontières)
- Thuan, T. X., & Izotov, Y. I. 2004, *ApJ*, submitted
- Thuan, T. X., Lecavelier des Etangs, A., & Izotov, Y. I. 2002, *ApJ*, 565, 941
- Thuan, T. X., Lipovetsky, V. A., Martin, J.-M., & Pustilnik, S. A. 1999, *A&AS*, 139, 1
- Thuan, T. X., & Martin, G. E. 1981, *ApJ*, 247, 823 (TM81)
- Thuan, T. X., Williams, T. B., & Malumuth, E. 1987, in *Starbursts and Galaxy Evolution*, ed. T. X. Thuan, T. Montmerle, & J. T. T. Van (Gif-sur-Yvette: Ed. Frontières), 151
- Tikhonov, N. A., Bilkina, B. I., Karachentsev, I. D., & Goergiev, T. B. 1991, *A&AS*, 89, 1
- Tolstoy, E., Saha, A., Hoessel, J. G., & McQuade, K. 1995, *AJ*, 110, 1640
- Toomre, A. 1964, *ApJ*, 139, 1217
- van Zee, L., Maddalena, R. J., Haynes, M. P., Hogg, D. E., & Roberts, M. S. 1997, *AJ*, 113, 1638
- van Zee, L., Skillman, E. D., & Salzer, J. J. 1998a, *AJ*, 116, 1186
- van Zee, L., Westpfahl, D., Haynes, M. P., & Salzer, J. J. 1998b, *AJ*, 115, 1000
- Viallefond, F., Lequeux, J., & Comte, G. 1987, in *Starbursts and Galaxy Evolution*, ed. T. X. Thuan, T. Montmerle, & J. T. T. Van (Gif-sur-Yvette: Ed. Frontières), 139
- Viallefond, F., & Thuan, T. X. 1983, *ApJ*, 269, 444
- Weaver, R., McCray, R., Castor, J., Shapiro, P., & Moore, R. 1977, *ApJ*, 218, 377
- Wevers, B. M. H. R., van der Kruit, P. C., & Allen, R. J. 1986, *A&AS*, 66, 505
- Wilcots, E. M., Lehman, C., & Miller, B. 1996, *AJ*, 111, 1575
- Wolfire, M. G., Hollenback, D., McKee, C. F., Tielens, A. G., & Bakes, E. L. O. 1995, *ApJ*, 443, 152
- Young, L. M., van Zee, L., Lo, K. Y., Dohm-Palmer, R. C., & Beierle, M. E. 2003, *ApJ*, 592, 111